

NASA

IN-34
394 483
p.64

MEMORANDUM

INCLINED BODIES OF VARIOUS CROSS SECTIONS

AT SUPERSONIC SPEEDS

By Leland H. Jorgensen

Ames Research Center
Moffett Field, Calif.

NATIONAL AERONAUTICS AND
SPACE ADMINISTRATION

WASHINGTON

November 1958

Declassified May 29, 1961

NATIONAL AERONAUTICS AND SPACE ADMINISTRATION

NASA MEMO 10-3-58A

INCLINED BODIES OF VARIOUS CROSS SECTIONS

AT SUPERSONIC SPEEDS *

By Leland H. Jorgensen

SUMMARY

To aid in assessing effects of cross-sectional shape on body aerodynamics, the forces and moments have been measured for bodies with circular, elliptic, square, and triangular cross sections at Mach numbers 1.98 and 3.88. Results for bodies with noncircular cross sections have been compared with results for bodies of revolution having the same axial distribution of cross-sectional area (and, thus, the same equivalent fineness ratio). Comparisons have been made for bodies of fineness ratios 6 and 10 at angles of attack from 0° to about 20° and for Reynolds numbers, based on body length, of 4.0×10^6 and 6.7×10^6 .

The results of this investigation show that distinct aerodynamic advantages can be obtained by using bodies with noncircular cross sections. At certain angles of bank, bodies with elliptic, square, and triangular cross sections develop considerably greater lift and lift-drag ratios than equivalent bodies of revolution. For bodies with elliptic cross sections, lift and pitching-moment coefficients can be correlated with corresponding coefficients for equivalent circular bodies. It has been found that the ratios of lift and pitching-moment coefficients for an elliptic body to those for an equivalent circular body are practically constant with change in both angle of attack and Mach number. These lift and moment ratios are given very accurately by slender-body theory. As a result of this agreement, the method of NACA Rep. 1048 for computing forces and moments for bodies of revolution has been simply extended to bodies with elliptic cross sections. For the cases considered (elliptic bodies of fineness ratios 6 and 10 having cross-sectional axis ratios of 1.5 and 2), agreement of theory with experiment is very good.

As a supplement to the force and moment results, visual studies of the flow over bodies have been made by use of the vapor-screen, sublimation, and white-lead techniques. Photographs from these studies are included in the report.

*Title, Unclassified.

INTRODUCTION

For missiles and airplanes designed for operation at supersonic speeds, the aerodynamic characteristics of the bodies are often very important. Although there are data and theoretical methods available from which the aerodynamics for bodies of revolution to high angles of attack can be determined, there is little information for highly inclined bodies of noncircular cross section. Data are available for cones of elliptic cross section at angles of attack to 16° (ref. 1). For other noncircular bodies most aerodynamic knowledge comes from experimental results for bodies at low angles of attack (ref. 2) and from slender-body theory (e.g., ref. 3). Primarily because of failure to consider effects of viscosity in the flow, slender-body theory is limited to slender bodies at very low angles of attack. However, from this theory there is the indication that important aerodynamic advantages can result from use of bodies of noncircular cross section instead of bodies of revolution. For example, it can be shown that bodies with elliptic, square, or triangular cross sections develop higher values of lift and lift-drag ratio than equivalent bodies of revolution having the same axial distribution of cross-sectional area.

To provide additional experimental data from which to evaluate the theoretical advantages of noncircular bodies, the present investigation was undertaken. For Mach numbers of 1.98 and 3.88, aerodynamic forces and moments were measured for bodies with circular, elliptic, square, and triangular cross sections at angles of attack from 0° to about 20° . The purpose of this report is to discuss the resulting aerodynamic data and to compare theoretical and experimental results.

NOTATION

A_b	body base area
A_p	body plan-form area
a	semimajor axis of elliptic cross section
b	semiminor axis of elliptic cross section
C_{d_c}	section drag coefficient of circular cylinder, based on cylinder diameter
C_D	drag coefficient, $\frac{D}{q_\infty A_b}$
C_{D_0}	drag coefficient at zero lift

C_L	lift coefficient, $\frac{L}{q_\infty A_b}$
$(C_L)_{a/b=1}$	lift coefficient for equivalent body of revolution
C_m	pitching-moment coefficient about base of body, $\frac{\text{pitching moment}}{q_\infty A_b l}$
$(C_m)_{a/b=1}$	pitching-moment coefficient about base of equivalent body of revolution
D	drag (exclusive of base drag)
d	body base diameter
l	body length
L	lift
$\left(\frac{L}{D}\right)_{\max}$	maximum lift-drag ratio
$\left[\left(\frac{L}{D}\right)_{\max}\right]_{a/b=1}$	maximum lift-drag ratio for equivalent body of revolution
M_∞	free-stream Mach number
Q	body volume
q_∞	free-stream dynamic pressure
R	Reynolds number based on body length
x, y, z	Cartesian coordinates as shown in figure 1
x_c	axial distance from nose vertex to centroid of plan- form area
x_m	axial distance from nose vertex to pitching-moment reference center
x_p	center of pressure measured from nose vertex
α	angle of attack measured between body longitudinal axis and free-stream direction (see fig. 1)
ϕ	angle of bank about body longitudinal axis (see fig. 1)

The positive directions of the angles and coefficients are shown in figure 1.

APPARATUS AND TESTS

Wind Tunnel

The experimental investigation was conducted in the Ames 1- by 3-foot supersonic wind tunnel No. 1. This tunnel is a closed-circuit, continuous-operation type and is equipped with a flexible-plate nozzle that provides a variation of Mach number from 1.4 to 4.0. The Reynolds number is changed by varying the total pressure within the approximate limits of $1/5$ of an atmosphere to 4 atmospheres.

Except for vapor-screen tests, the water content of the air in the tunnel is maintained at less than 0.0003 pound of water per pound of dry air. Consequently, the effect of humidity on the flow is negligible.

Models

Sketches of the bodies oriented as they were tested are shown in figure 2. Body B_1 , which had a circular cross section, consisted of a circular-arc tangent ogive nose of fineness ratio 3 with a cylindrical afterbody 7 diameters long. Bodies B_2 through B_5 , which had elliptic ($a/b = 1.5$ and 2), square, and triangular cross sections, all had the same length and axial distribution of cross-sectional area as B_1 . Hence, the fineness ratio of $l/d = 10$ for B_1 was also the equivalent fineness ratio for B_2 through B_5 . Body B_6 , which had a circular cross section, was identical to B_1 except for a shorter cylindrical afterbody resulting in a total fineness ratio of 6. Body B_7 with an elliptic cross section ($a/b = 2$), was the same length as B_6 and had the same axial distribution of cross-sectional area.

All of the bodies were constructed of steel and were supported from the rear on a strain-gage balance.

Tests

Force tests.- Balance measurements of lift, drag, and pitching moment were obtained for all the bodies at a free-stream Mach number of 1.98. Data also were obtained for bodies B_1 , B_3 , B_4 , and B_5 at a Mach number of 3.88. For the fineness-ratio-10 bodies (B_1 through B_5) the Reynolds number, based on body length, was 6.7×10^6 , and for the fineness-ratio-6 bodies (B_6 and B_7) the Reynolds number was 4.0×10^6 . The angle-of-attack range was from 0° to about 22° for the bodies at Mach number 1.98 and from 0° to about 15° for the bodies at Mach number 3.88. Tests were made with the bodies oriented as shown in figure 2. Base pressures from eight orifices spaced around the inside

of the base periphery of each model were measured from photographic recordings of a multiple-tube manometer board. In addition to the force tests, visual-flow tests, as discussed in the following paragraphs, were made for the fineness-ratio-10 bodies at Mach numbers 1.98 and 3.88.

Vapor-screen tests.- To make visible the vortices which are shed from the models at angle of attack, the "vapor-screen" method (refs. 1 and 4) was used. With this technique, water vapor is added to the tunnel air stream. This water vapor condenses in the wind-tunnel test section to produce a fine fog. A thin sheet of bright light, produced by high-intensity mercury-vapor lamps, is projected through the tunnel window in a plane perpendicular to the model longitudinal axis. This plane of light appears as a uniformly lighted screen of fog particles in the absence of a model. However, with a model in the stream, the flow about the model affects the light scattered by the water particles, and vortices shed from the model are visible as dark spots. For the present investigation, the vortex patterns for various bodies at angle of attack were photographed with a camera mounted inside the wind tunnel on the model sting support. The camera lens was positioned about 13 inches downstream from the base of the models.

Sublimation tests.- The sublimation technique (ref. 5) was used for determining the position of boundary-layer transition. The models, which were initially painted black, were sprayed with an 8-percent solution of biphenyl in petroleum ether. This solution dries on contact with the model surface and presents a white appearance. As the wind tunnel is operated, the process of sublimation takes place with turbulent boundary-layer regions showing up as dark areas on the model and laminar regions remaining white. (Solutions other than biphenyl in petroleum ether can be used to produce different rates of sublimation for various tunnel operating conditions. For example, a saturated solution of tetrachlorobenzene in benzene results in a much faster rate, while acenaphthene or azobenzene in petroleum ether results in a slower rate.)

White-lead tests.- Flow patterns on the models at angles of attack were visualized through use of a liquid-film technique. The models were painted with a mixture of white lead and light lubricating oil (S.A.E. 10) and were run wet in the wind tunnel. With a model at a desired angle of attack, flow directions and regions of separation became discernible on the surface, as will be discussed later. Tests were made for the fineness-ratio-10 models at angles of attack of 10° and 14° .

REDUCTION AND ACCURACY OF DATA

All of the force and moment data have been reduced to coefficient form and are referred to the coordinate system shown in figure 1. The

average base pressure was used to compute the base drag which was subtracted from the total axial-force balance measurement, so that the data presented are for forces ahead of the body base.

The accuracy of the final data is affected by uncertainties in the measurement of the forces and moments, and in the determination of the stream static and dynamic pressures used in reducing the forces and moments to coefficient form. These individual uncertainties led to estimated uncertainties which are listed below.

C_L	± 0.03
C_D	$\pm .008$
C_m	$\pm .03$
L/D	$\pm .1$
x_p/l	$\pm .02$

The values of angle of attack are estimated to be accurate to within $\pm 0.1^\circ$. The variation of the free-stream Mach number in the region of the test models was less than ± 0.01 at Mach number 1.98 and less than ± 0.02 at Mach number 3.88.

RESULTS AND DISCUSSION

In this section of the report the effect of cross-sectional shape on the experimental aerodynamic characteristics is considered first. Next, a correlation of lift and pitching-moment data for noncircular bodies with corresponding data for equivalent bodies of revolution is presented. A method is then outlined for computing the aerodynamic characteristics for bodies with elliptic cross sections. This method is used in a comparison of theoretical and experimental characteristics. As a final part to this section of the report, results from visual-flow studies are presented and discussed.

Effect of Cross-Sectional Shape on Experimental Aerodynamic Characteristics

Bodies with elliptic cross sections.- Results showing the effect of change in cross-sectional axis ratio (a/b) on the aerodynamic characteristics for elliptic bodies at angles of bank of 0° and 90° are presented in figures 3, 4, and 5. In each figure data are compared for bodies with a/b 's from 1 to 2 which all have the same axial distribution of cross-sectional area and, hence, equivalent fineness ratio. Elevation and end-view sketches of the models banked as they were tested are used to identify each curve, a practice followed throughout the report. Note that increases in axis ratio (a/b) result in increases in plan-form area with the semimajor axis, a , horizontal, and decreases in plan-form area with the semiminor axis, b , horizontal. In view of this

fact, it is not surprising that with increase in a/b the lift coefficients (which are referred to base area) increase appreciably at all angles of attack with the semimajor axis, a , horizontal and decrease with the semiminor axis, b , horizontal. (See, e.g., fig. 3(a).) As will be shown later, for the major axis horizontal ($\varphi=0^\circ$) the lift coefficients at a given angle of attack increase almost in direct proportion with increase in a/b . The question arises, then, of whether or not the aerodynamic efficiency as determined by lift-drag ratio also can be markedly increased by increasing a/b . From figures 3(c), 4(c), and 5(c) it is clear that, at least throughout the angle-of-attack range investigated, significant gains in lift-drag ratio can be realized. In fact, merely increasing a/b from 1 to 1.5 results in a gain in maximum L/D of about 16 percent for fineness-ratio-10 bodies at 0° bank and at $M_\infty = 1.98$ (fig. 3(c)). Furthermore, increasing a/b from 1 to 2 results in about a 32-percent increase in maximum L/D for fineness-ratio-10 bodies and in about a 37-percent increase for fineness-ratio-6 bodies at $M_\infty = 1.98$ (figs. 3(c) and 4(c)). Increasing a/b from 1 to 2 at the higher Mach number of 3.88 results in a gain in maximum L/D of about 26 percent (fig. 5(c)). It is also interesting to note that, for a given body, lift-drag ratio increases with increase in Mach number. An explanation for this behavior is given further on in the report.

The effect of axis ratio on center of pressure and pitching moment is shown in parts (d) and (e) of figures 3, 4, and 5. For all the bodies, the center of pressure is on the nose section for angles of attack near zero and then moves rearward on the body with increase in angle of attack. The center-of-pressure positions for the elliptic bodies at each angle of attack are, for the most part, fairly close to those for the equivalent bodies of revolution.

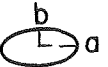
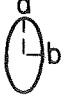
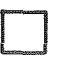



Bodies with circular, square, and triangular cross sections.-
Aerodynamic characteristics for fineness-ratio-10 bodies with circular, square, and triangular cross sections are compared in figure 6 for $M_\infty = 1.98$ and in figure 7 for $M_\infty = 3.88$. The comparisons clearly show that throughout the angle-of-attack range the bodies with square and triangular cross sections develop greater lift than the equivalent circular body at the same inclination (figs. 6(a) and 7(a)). This result applies for the square and triangular bodies oriented either with a flat side underneath and windward or banked so that only one corner is underneath. At a given Mach number and angle of attack the triangular body develops the greatest lift, the lifting capability being highest with the body oriented with a flat side underneath. For the square body the greater lift is developed with the body banked so that a corner is underneath. Except for the square body oriented with a flat side below, the noncircular bodies also produce higher lift-drag ratios than the circular (figs. 6(c) and 7(c)). However, the circular body has the advantage of less drag at zero lift, especially at Mach number 3.88 (figs. 6(b) and 7(b)). This is probably due, at least in part, to less skin-friction drag resulting from less wetted area and more laminar flow. As will be shown later, considerably more laminar flow was obtained over the circular bodies than over the noncircular.

The center-of-pressure positions for the noncircular bodies are generally a little rearward from those for the circular body (figs. 6(d) and 7(d)). It is interesting to note, however, that the center-of-pressure positions for the noncircular bodies move closer to those for the circular body with increase in Mach number from 1.98 to 3.88. This trend with Mach number was also observed for the elliptic bodies.

Correlation of Lift and Pitching-Moment Results

Although the lift and pitching-moment results for all the elliptic bodies show nonlinear variation with α , the data can be simply correlated as shown in figure 8. Here the lift and pitching-moment coefficients for the elliptic bodies are divided by the corresponding coefficients for the equivalent circular body, and the ratios are plotted as a function of α . The results of the correlation demonstrate that, in general, $C_L/(C_L)_{a/b=1}$ and $C_m/(C_m)_{a/b=1}$ remain constant with changes in α and are practically independent of fineness ratio and Mach number. (A similar correlation for cones with elliptic cross sections is reported in ref. 1. Data from ref. 2 for an elliptic body also can be correlated to give the same result.) It is important to note that, at least for all conditions of this investigation, the lift and moment ratios are given very closely by slender-body theory. In fact, the maximum disagreement between theory and experiment at any angle of attack considered is no greater than about 10 percent.

For slender bodies the ratios $C_L/(C_L)_{a/b=1}$ and $C_m/(C_m)_{a/b=1}$ for various polygonal cross sections can be determined using the coefficients of apparent mass reported in reference 6. Theoretical ratios for the cross sections considered in the present investigation are summarized in the following table:

Cross section	Orientation	$\frac{C_L}{(C_L)_{a/b=1}} = \frac{C_m}{(C_m)_{a/b=1}}$
Ellipse		$\frac{a}{b}$
Ellipse		$\frac{b}{a}$
Square	 or 	1.19
Triangle	 or 	1.58

In figure 9 results are presented of an attempt to correlate data for bodies with square and triangular cross sections with data for an equivalent body of circular cross section. Although the correlations for elliptic bodies previously shown in figure 8 are very good, the correlations for the triangular and square bodies are generally poor, except for the square body oriented with a flat side underneath. However, for some reason, as yet unexplained, the correlations and the agreement of theory with experiment improve with increase in Mach number from 1.98 to 3.88.

Method for Computing Aerodynamic Characteristics for Bodies With Elliptic Cross Sections

Because of close agreement of theoretical and experimental values of $C_L/(C_L)_{a/b=1}$ and $C_m/(C_m)_{a/b=1}$, the aerodynamic characteristics for bodies with elliptic cross sections can be readily determined if the characteristics for equivalent bodies of revolution are known. Allen (ref. 4) proposes a theory for predicting the forces and moments for slender bodies of revolution inclined to angles of attack considerably higher than those for which theories based only on potential-flow concepts are known to apply. In this theory an additional crossflow lift attributed to the separation effects of viscosity is added to the lift predicted by potential theory. The viscous crossflow is considered to be independent of the axial flow and to be that of the steady flow past a circular cylinder. Although this theory is semiempirical in that experimental crossflow drag coefficients for circular cylinders are used, it has provided considerable improvement over potential theory for computing forces and moments for bodies which have cylindrical aftersections of constant diameter.

For bodies of revolution the equations for lift coefficient and pitching-moment coefficient are

$$(C_L)_{a/b=1} = 2\alpha + C_{d_c} \frac{A_p}{A_b} \alpha^2 \quad (1)$$

and

$$(C_m)_{a/b=1} = 2 \left[\frac{Q - A_b(l - x_m)}{A_b l} \right] \alpha + C_{d_c} \frac{A_p}{A_b} \left(\frac{x_m - x_c}{l} \right) \alpha^2 \quad (2)$$

where

Q body volume

- A_b body base area (reference area for coefficient evaluation)
 A_p body plan-form area
 x_c axial distance from nose vertex to centroid of plan-form area
 x_m axial distance from nose vertex to pitching-moment reference center
 l body length

and C_{d_c} is the section drag coefficient for a two-dimensional circular cylinder placed normal to a stream at a Mach number of $M_\infty \sin \alpha$. In equations (1) and (2) the potential components are given by the first term and the viscous, by the second.

If the lift for a body of revolution can be considered to be the summation of a potential-flow lift and a viscous-flow lift, it is reasonable to expect that the same concept can apply for bodies with elliptic cross sections. From slender-body theory, the ratio of the potential-flow lift for an elliptic body to that for an equivalent circular body is given by

$$\frac{C_L}{(C_L)_{a/b=1}} = \frac{C_m}{(C_m)_{a/b=1}} = \frac{a}{b} \cos^2 \varphi + \frac{b}{a} \sin^2 \varphi \quad (3)$$

where φ is the angle of bank about the body longitudinal axis, being equal to 0° with the semimajor axis, a , horizontal, and 90° with the semiminor axis, b , horizontal. The close agreement of theoretical and experimental values of $C_L/(C_L)_{a/b=1}$, shown in correlations of figure 8, indicates that the viscous crossflow components of lift for the elliptic and circular bodies are also closely related by the same simple expression. For bodies with elliptic cross sections, the lift and pitching-moment coefficients can be computed by means of equations (1), (2), and (3). The drag coefficients can be estimated by means of the relation

$$C_D = C_{D_0} + C_L \alpha \quad (4)$$

where C_{D_0} is the zero-lift drag coefficient for the body considered.

Comparisons of Theoretical and Experimental Aerodynamic Characteristics for Bodies With Elliptic Cross Sections

Theoretical and experimental aerodynamic characteristics for elliptic bodies at Mach numbers 1.98 and 3.88 are compared in figures 10 through 13. In general, the theoretical curves, which were determined in accordance with the method previously outlined, are in very good agreement with the experimental results. In the computations of the lift and pitching-moment characteristics from equations (1), (2), and (3), values of C_{d_c} (which varied from about 1.2 to 1.6 depending on $M_\infty \sin \alpha$) were taken from reference 7. In the computations of the drag characteristics from equation (4), the zero-lift drag coefficient, C_{D_0} , was taken as the sum of the skin-friction and pressure-drag coefficients. Since there is no method for readily computing the pressure drag of elliptic bodies, the zero-lift drag coefficients for these bodies were assumed to be equal to those computed for the equivalent bodies of revolution. (This assumption is approximately substantiated by experimental results.) From sublimation tests it was observed that the boundary-layer flow for the circular bodies was laminar over about the forward 6 diameters of body length and turbulent over the rest of the body. (See fig. 18.) Hence, for the bodies of revolution considered, laminar skin-friction drag (ref. 8) for the forward 6 diameters of body length was added to turbulent skin-friction drag (ref. 9) for the remaining length. The pressure drag was determined from reference 10, having been originally computed by the method of characteristics.

In figure 13 it is interesting to note the close agreement of theory with experiment for the variation of $(L/D)_{\max}$ with a/b . This agreement indicates the reliability of using theory for determining relative efficiencies for elliptic bodies.

By comparing figure 13(a) with 13(c), it can be seen, as was mentioned previously, that $(L/D)_{\max}$ for a given body increases with increase in Mach number from 1.98 to 3.88. This increase is explainable from theory. At the angles of attack for $(L/D)_{\max}$, the body crossflow drag coefficients C_{d_c} (which vary with $M_\infty \sin \alpha$) are higher for $M_\infty = 3.88$ than for $M_\infty = 1.98$, and hence the lift coefficients are also higher (see eq. (1)). At the same time, the drag coefficients (see eq. (4)) are reduced, since both the pressure and skin-friction drag coefficients which are added together to give C_{D_0} decrease with increase in Mach number. At Mach numbers greater than about 6 a decrease in $(L/D)_{\max}$ might occur, since C_{d_c} decreases with increase in $M_\infty \sin \alpha$ for values greater than about 1.

Visual Observations of Flow Over Models

To supplement the force and moment results with studies that aid in giving a physical representation of the flow, vapor-screen, sublimation, and white-lead tests were made for the bodies at $M_0 = 1.98$ and 3.88 . Photographs of the resulting flow patterns are presented in figures 14 through 21. As mentioned previously, the vapor-screen pictures were taken with a camera mounted inside the tunnel 13 inches downstream of the models. The pictures of the models from the sublimation and white-lead tests were taken immediately following tunnel shutdown.

Vapor-screen results.- In the photographs of figure 14, vortices shed from circular and elliptic bodies at $M_0 = 1.98$ and angles of attack from 5° to 17° are shown. For the rear views in figure 14(a), the vapor-screen light plane intersected the bodies at $x = 5d$, and for the rear views in figure 14(b), the light plane was at the body base ($x = 10d$). The flow appears to separate near the sides of the circular and elliptic bodies, and at angles of attack greater than about 5° a symmetrical pair of vortices become discernible. (The shadow to the right of each body should be disregarded in studying the photographs.) The sizes of the vortices (and presumably the strengths) increase both with increase in α and with travel rearward to the body base. The vortex regions, as expected, also move outboard relative to the body vertical center line with increase in a/b from 1 to 2.

In figure 15 vortex patterns for bodies with circular, square, and triangular cross sections are compared. These photographs were taken with the bodies at angles of attack from 5° to 17° and for $M_0 = 1.98$. At an axial distance of 5 diameters from the nose vertex, separation takes place near the sides of the circular and elliptic bodies (fig. 15(a)). However, for the square body B_4 with a flat side windward, the flow appears to separate near the top. At the rear of the square body (fig. 15(b)) additional regions of vorticity appear on the left side of the body. Actually, separation regions appeared on both sides of the body, but probably because of slight misalignment of the body with the tunnel air stream, the vortex regions were larger on the left side than on the right. With the square body banked 45° , flow separation occurs near the side corners, as might be expected. For the triangular body B_5 oriented with a flat side windward, separation appears to take place near the bottom corners, whereas with the body banked so that a flat side is leeward, separation occurs at the top corners, and the vortices pass above the body at all angles of attack. In all cases studied for $\alpha = 5^\circ$, the vortices for the square and triangular bodies are more discernible and appear to be more completely rolled up than those for the circular and elliptic bodies. For all bodies the vortices increase in size with increase in α and with travel rearward.

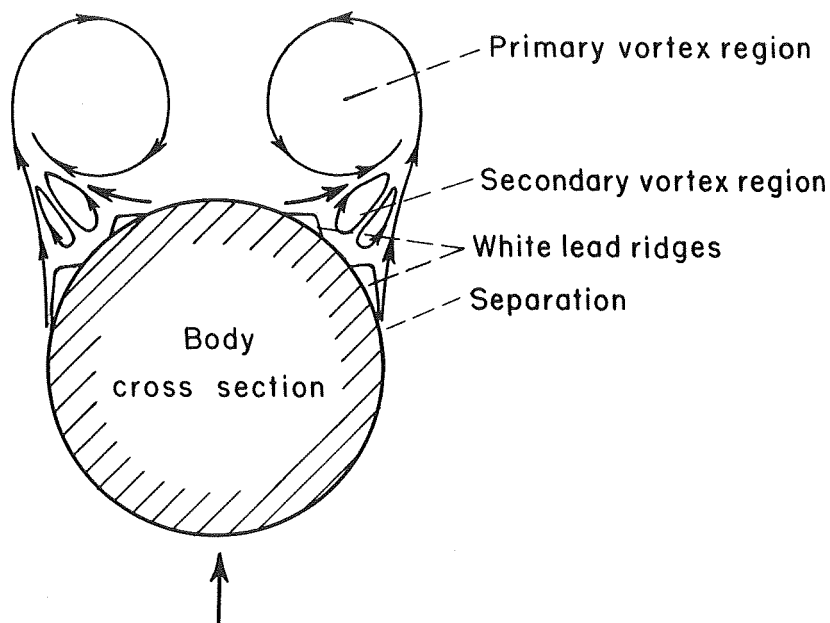
The effect on the vortex regions of change in Mach number from 1.98 to 3.88 is shown in figure 16. Photographs of vortex patterns for the

circular body B_1 and the $a/b = 2$ elliptic body B_3 at angles of attack to 14° are presented. It is readily apparent that, for a given body and angle of attack, the regions of vorticity are larger at $M_\infty = 3.88$ than at $M_\infty = 1.98$. The visual appearance of the vortex regions for the square and triangular bodies is also considerably different at $M_\infty = 3.88$ than at $M_\infty = 1.98$. This can be seen in a comparison of the results in figure 17 for $M_\infty = 3.88$ with those in figure 15 for $M_\infty = 1.98$. For a clear understanding of the effect of Mach number on vortex strength and the distribution of vorticity in the separated regions, pressure and stream-angle surveys of the body flow fields would be required.

Sublimation and white-lead results.- In order to obtain a visual indication of the flow on the surface of the bodies, the sublimation and white-lead techniques were used. In figure 18 photographs are presented of typical flow patterns on bodies at $\alpha = 0^\circ$ resulting from sublimation tests. The results are for $M_\infty = 1.98$ and $R = 6.7 \times 10^6$. Laminar-flow regions are white, and turbulent regions are black. It is interesting to note that the longest length of laminar run was obtained with the circular body B_1 , the flow being laminar over the forward 6 diameters of body length. With change in body cross section to elliptic, square, or triangular, the extent of laminar flow was markedly decreased. For all bodies there was no noticeable effect on transition due to increase in Mach number from 1.98 to 3.88. In testing the circular body, it was found that with only slight increase in α ($\alpha \approx 1^\circ$), the turbulent region extended to the nose vertex on the leeward side, and the laminar region diminished. With increase in α to angles greater than about 5° , indications of flow separation and vortex formation appeared on the body. Although the sublimation technique can be used to show these effects, the white-lead technique was found to be superior for revealing flow details and was used in this investigation.

Figures 19, 20, and 21 are photographs of the bodies taken following white-lead tests. Top, side, and bottom views are presented for bodies at $\alpha = 10^\circ$ and 14° for $M_\infty = 1.98$ (figs. 19 and 20), and for bodies at $\alpha = 14^\circ$ for $M_\infty = 3.88$ (fig. 21). In these pictures flow-separation positions are quite clearly defined. For the circular body B_1 and the elliptic body B_3 , separation starts at the top of the body at the nose vertex and then moves windward toward the sides of the body with distance downstream (see figs. 19(a) and (b) and 21(a) and (b)). At the separation line along the body there is a build-up or ridge of white lead formed. This is probably most clearly seen in figure 21(a). (Note that the white lead has started to run slightly in several regions of high concentration along the separation line. The photographs, however, are quite representative of the conditions observed with the bodies in the wind tunnel.) Leeward around the body from the separation ridge is a black bare area and then another ridge of white lead which results from the vortex flow. A typical representation of the crossflow over the

cylindrical portion of a circular body is shown in the sketch. The flow around the elliptic body is somewhat similar. However, for the square



and triangular bodies which have relatively sharp corners, flow separation takes place at or near the outermost corners, as was also observed from the vapor-screen results. With the square body at $\alpha = 14^\circ$ and oriented with a flat side windward, vortex flow was observed from the vapor-screen tests to take place on both sides of the body as well as on the top. See, for example, figures 15(b) and 17(b). The white-lead results shown in figures 19(c) and 21(c) substantiate the observation from the vapor-screen test. Although the vapor-screen results indicate differences in the shed vortex regions with change in Mach number from 1.98 to 3.88, the flow-separation positions on the bodies were practically unchanged. In general, the flow patterns on the bodies changed very little with increase in α from 10° to 14° , although the shed vortices increased in size.

It is interesting to observe that there is somewhat of an analogy between the visual-flow results and the lift correlations previously discussed. Flow separation for the elliptic bodies is quite similar in nature to that for the circular body and occurs at about the same body positions. Likewise, the lift forces for the elliptic bodies correlate well with those for the circular body. For the square and triangular bodies, flow separation is controlled by the body corners and is quite dissimilar to that for the circular body. Correlation of lift results for these bodies with those for the equivalent circular body is poor.

CONCLUSIONS

Aerodynamic characteristics for bodies with elliptic, square, and triangular cross sections have been measured and compared with results for equivalent bodies of revolution. Tests were made for bodies of fineness ratios 6 and 10 at Mach number 1.98 and for bodies of fineness ratio 10 at Mach number 3.88. The Reynolds number, based on body length, was 4.0×10^6 for the fineness-ratio-6 bodies and 6.7×10^6 for the fineness-ratio-10 bodies. The angle-of-attack range was from 0° to about 20° . An analysis of the results has led to the following conclusions:

1. Bodies with elliptic, square, or triangular cross sections develop higher values of lift and lift-drag ratio than equivalent bodies of revolution having the same axial distribution of cross-sectional area.

2. Lift and pitching-moment coefficients for bodies with elliptic cross sections can be correlated with corresponding coefficients for equivalent bodies of revolution. The ratios of lift and pitching-moment coefficients for an elliptic body to those for an equivalent circular body are practically constant with change in both angle of attack and Mach number. For bodies with square and triangular cross sections, no such simple correlation is known.

3. Ratios of lift coefficients and pitching-moment coefficients, resulting from correlation of data for bodies with elliptic and circular cross sections, are given closely by slender-body theory.

4. The method of NACA Rep. 1048 for computing forces and moments for bodies of revolution can be easily extended to compute aerodynamic characteristics for bodies with elliptic cross sections. For cases which have been considered, there is good agreement between theory and experiment.

Ames Research Center

National Aeronautics and Space Administration
Moffett Field, Calif., Aug. 20, 1958

REFERENCES

1. Jorgensen, Leland H.: Elliptic Cones Alone and With Wings at Supersonic Speeds. NACA TN 4045, 1957.
2. Carlson, Harry W., and Gapcynski, John P.: An Experimental Investigation at a Mach Number of 2.01 of the Effects of Body Cross-Section Shape on the Aerodynamic Characteristics of Bodies and Wing-Body Combinations. NACA RM L55E23, 1955.

3. Ward, G. N.: Supersonic Flow Past Slender Pointed Bodies. Quart. Jour. Mech. and Appl. Math., vol. II, pt. 1, Mar. 1949, pp. 75-97.
4. Allen, H. Julian, and Perkins, Edward W.: A Study of Effects of Viscosity on Flow Over Slender Inclined Bodies of Revolution. NACA Rep. 1048, 1951.
5. Main-Smith, J. D.: Chemical Solids as Diffusible Coating Films for Visual Indications of Boundary-Layer Transition in Air and Water. R.&M. 2755, British A.R.C., 1954.
6. Kuerti, G., McFadden, J. A., and Shanks, D.: Virtual Mass of Cylinder with Radial Fins and of Polygonal Prisms. NAVORD Rep. 2295, Aeroballistic Res. Rep. 61, Jan. 29, 1952.
7. Gowen, Forrest E., and Perkins, Edward W.: Drag of Circular Cylinders for a Wide Range of Reynolds Numbers and Mach Numbers. NACA TN 2960, 1953.
8. Blasius, H.: Grenzschichten in Flüssigkeiten mit Kleiner Reibung. Zeitschrift für Mathematik und Physik, vol. 56, no. 1, 1908, pp. 1-37.
9. Rubesin, Morris W., Maydew, Randall C., and Varga, Steven A.: An Analytical and Experimental Investigation of the Skin Friction of the Turbulent Boundary Layer on a Flat Plate at Supersonic Speeds. NACA TN 2305, 1951.
10. Rossow, Vernon J.: Applicability of the Hypersonic Similarity Rule to Pressure Distributions which Include the Effects of Rotation for Bodies of Revolution at Zero Angle of Attack. NACA TN 2399, 1951.

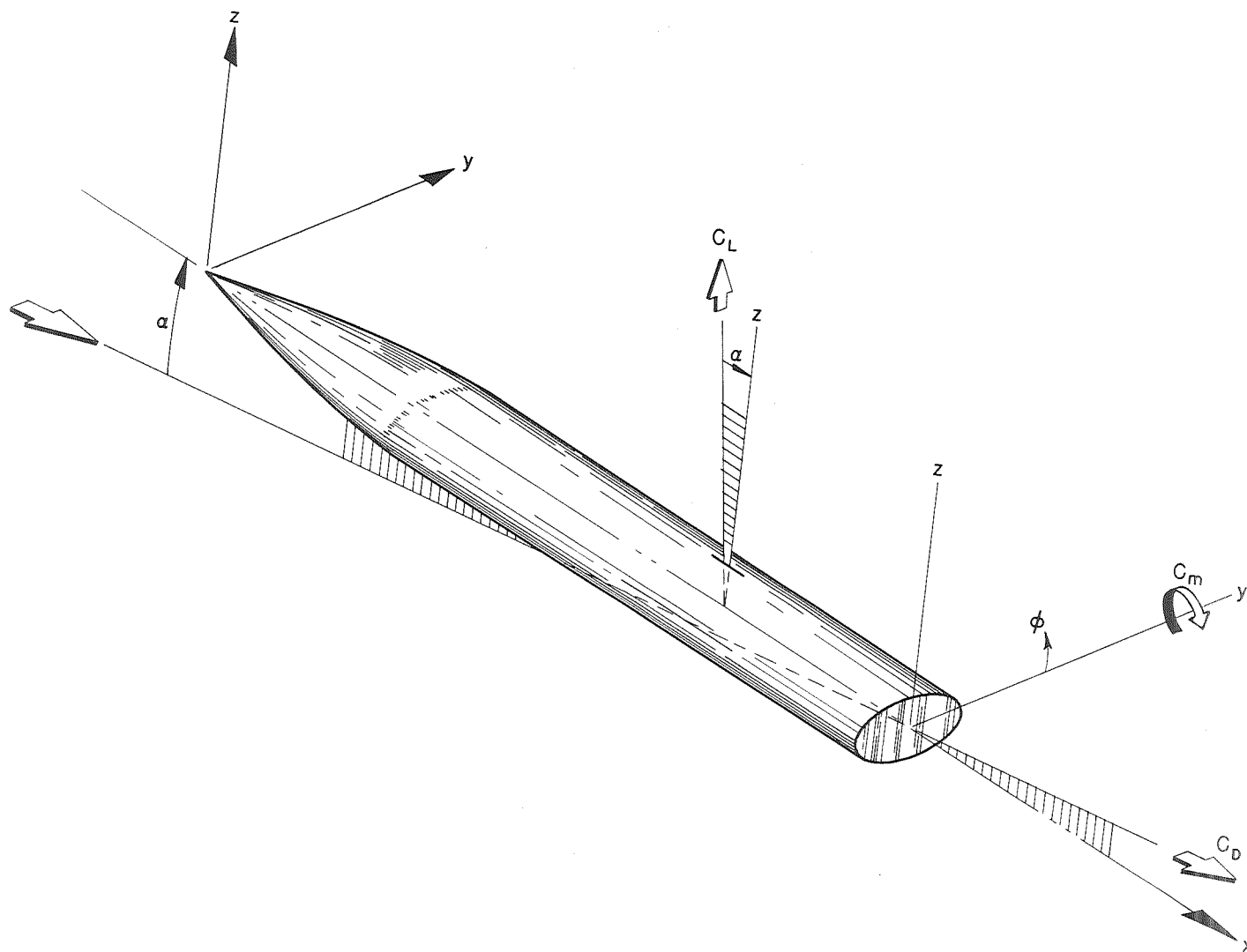


Figure 1.- Coordinate system and sign convention.

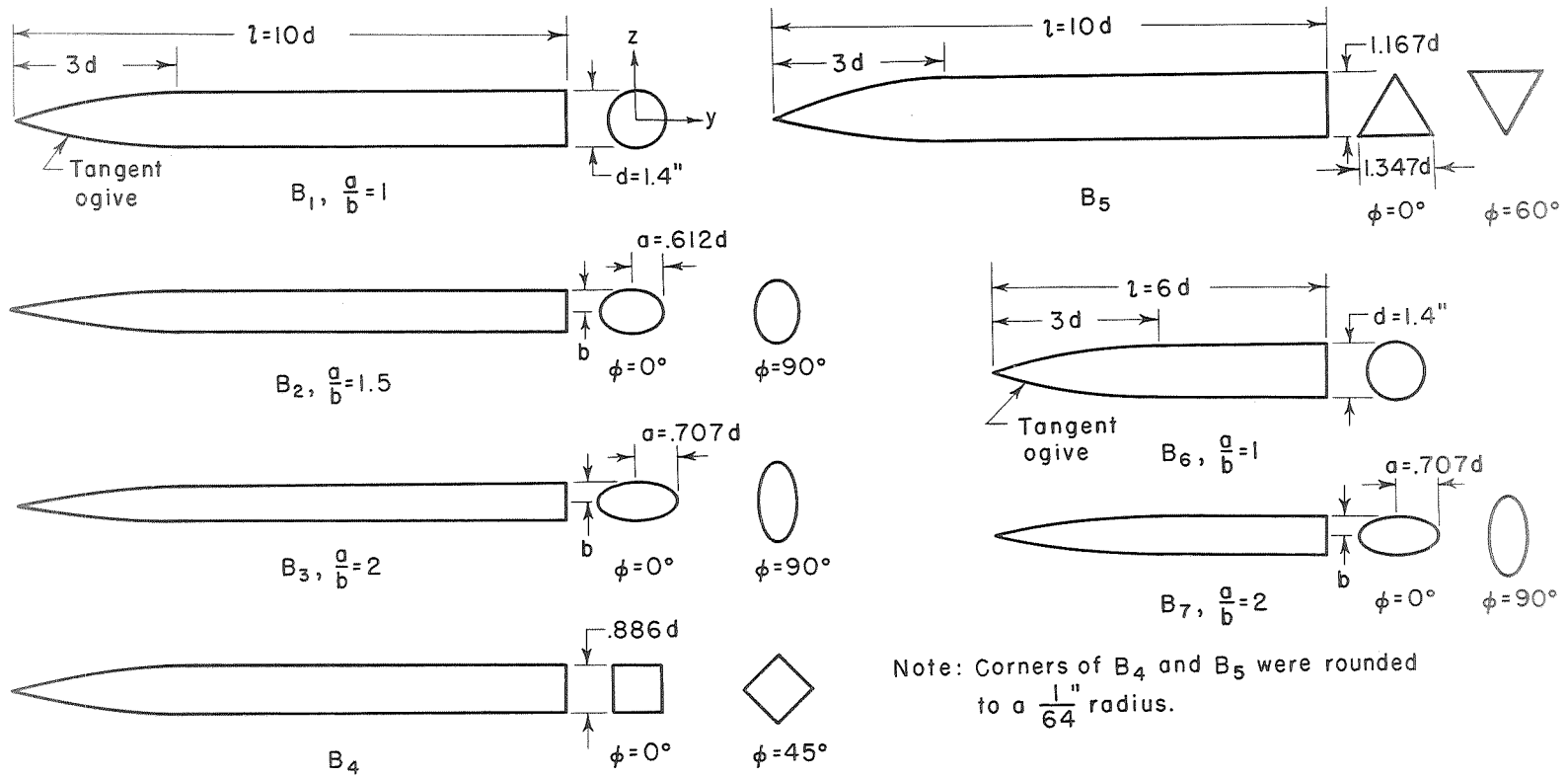


Figure 2.- Sketches and orientations of bodies tested.

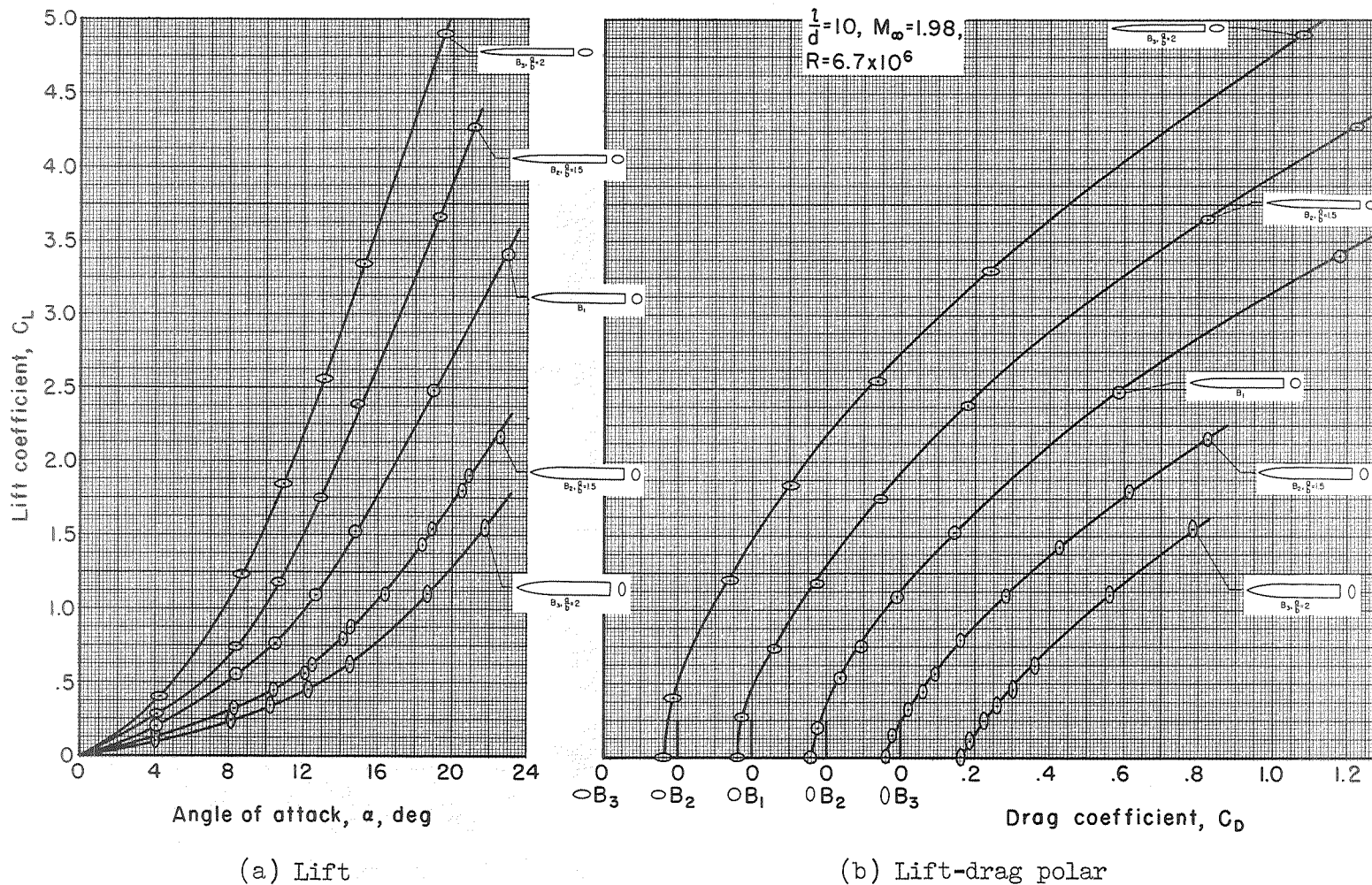
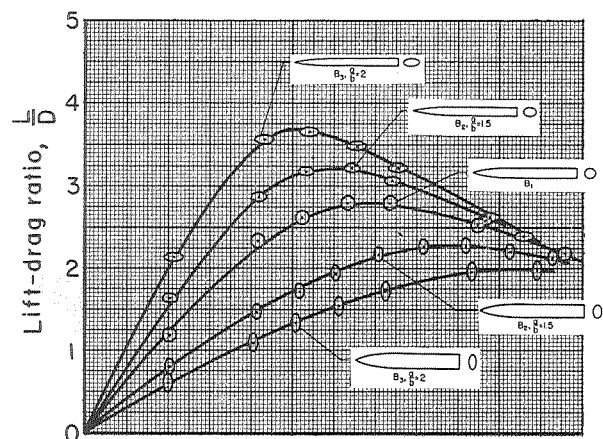
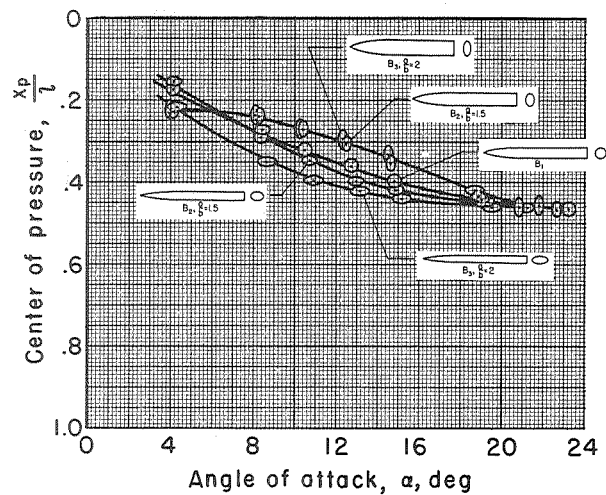


Figure 3.- Effect of change in axis ratio (a/b) on the aerodynamic characteristics for bodies with elliptic cross sections; $l/d = 10$, $M_\infty = 1.98$, $R = 6.7 \times 10^6$.

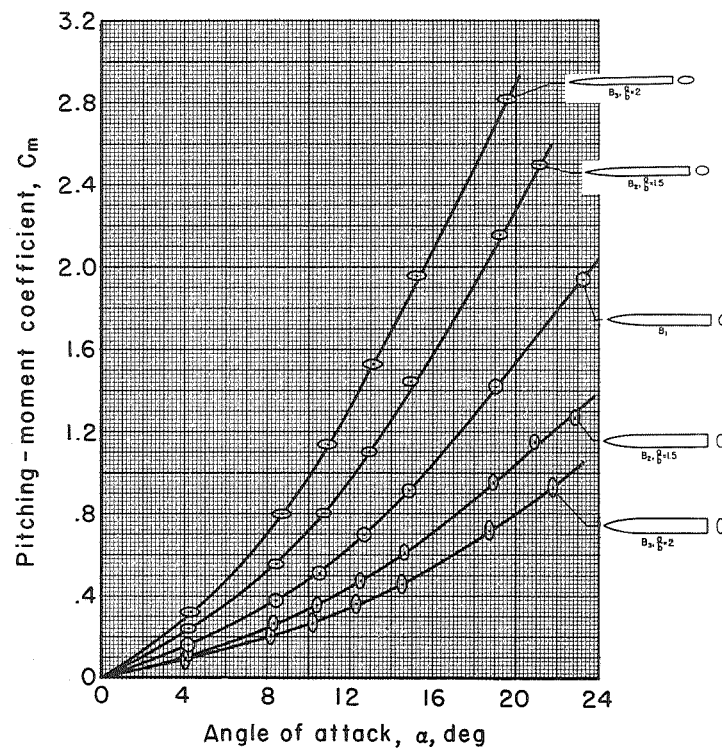


(c) Lift-drag ratio



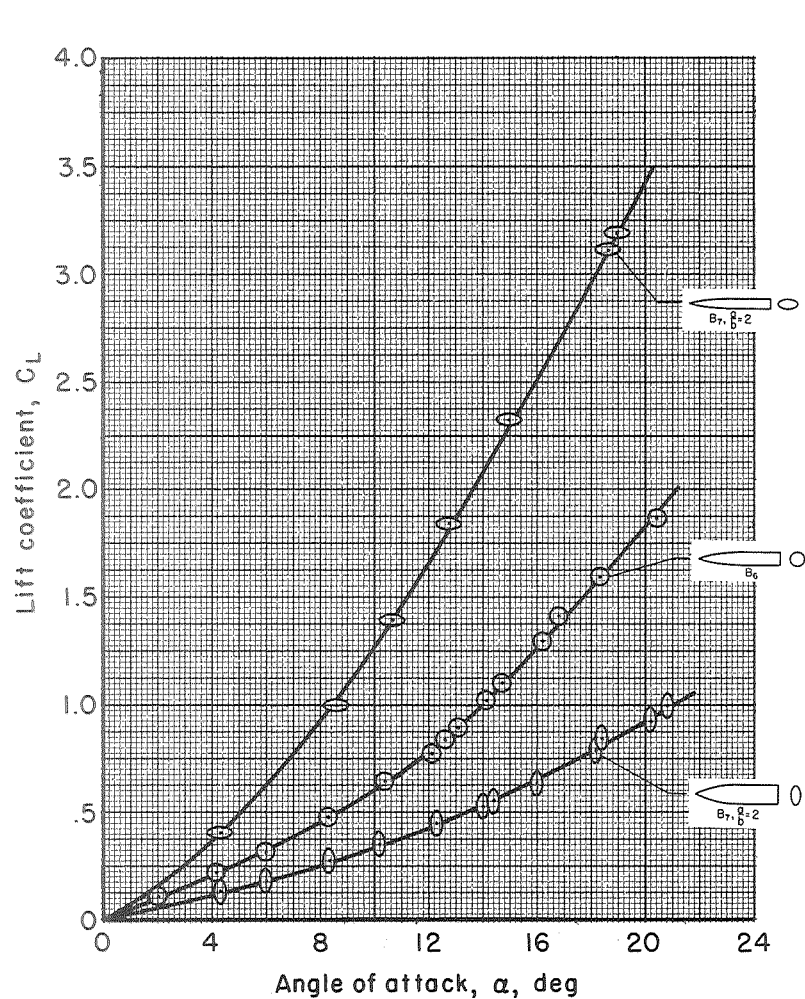
(d) Center of pressure

$$\frac{l}{d}=10, M_\infty=1.98, \\ R=6.7 \times 10^6$$

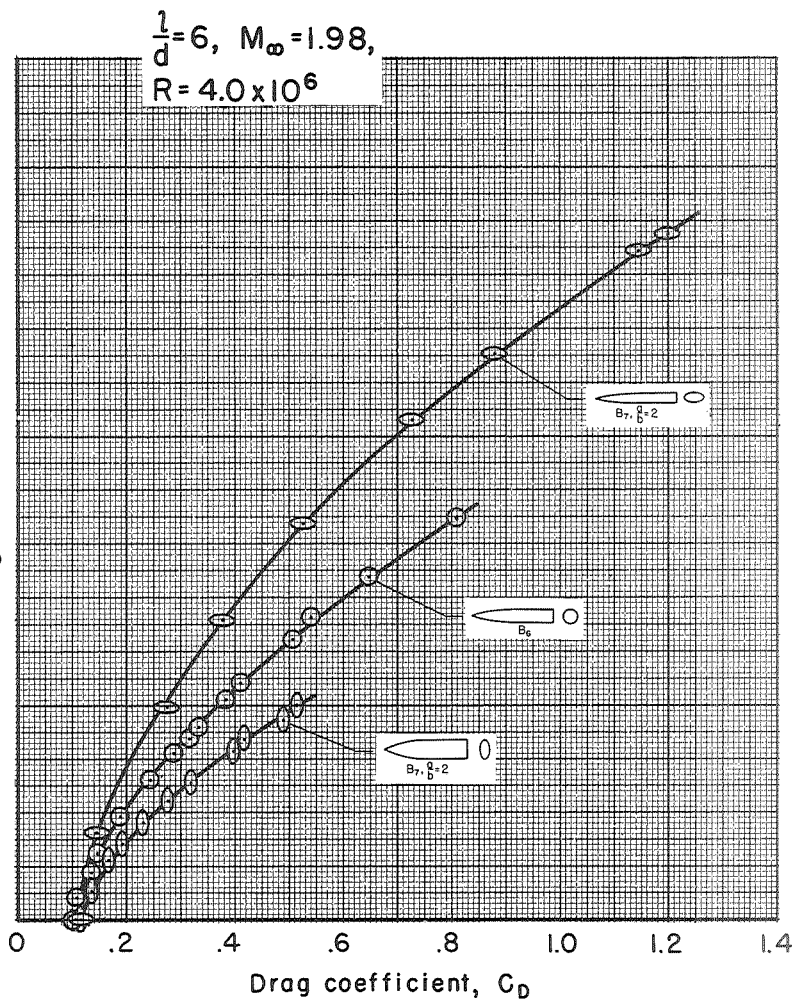


(e) Pitching moment

Figure 3.- Concluded.

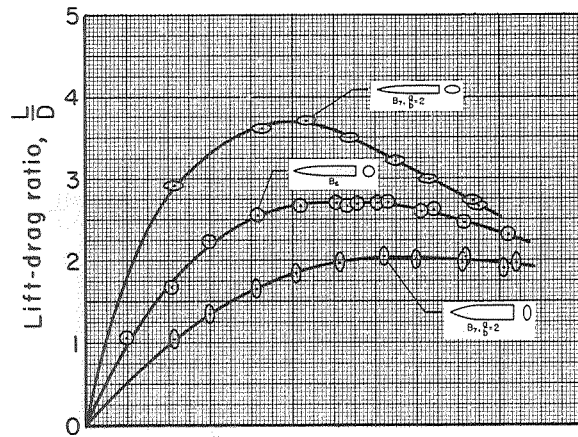


(a) Lift

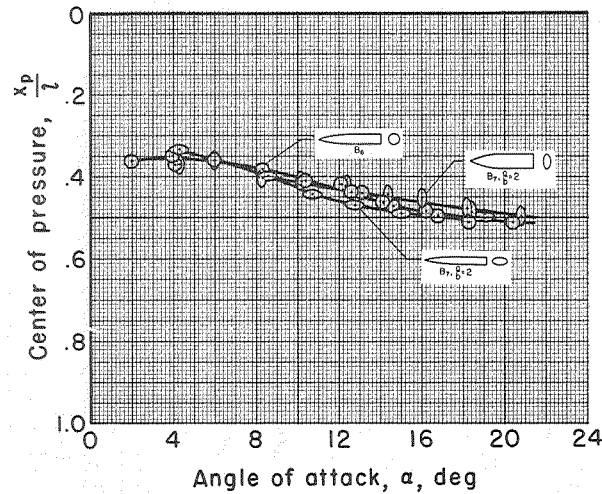


(b) Lift-drag polar

Figure 4.- Effect of change in axis ratio (a/b) on the aerodynamic characteristics for bodies with elliptic cross sections; $l/d = 6$, $M_\infty = 1.98$, $R = 4.0 \times 10^6$.

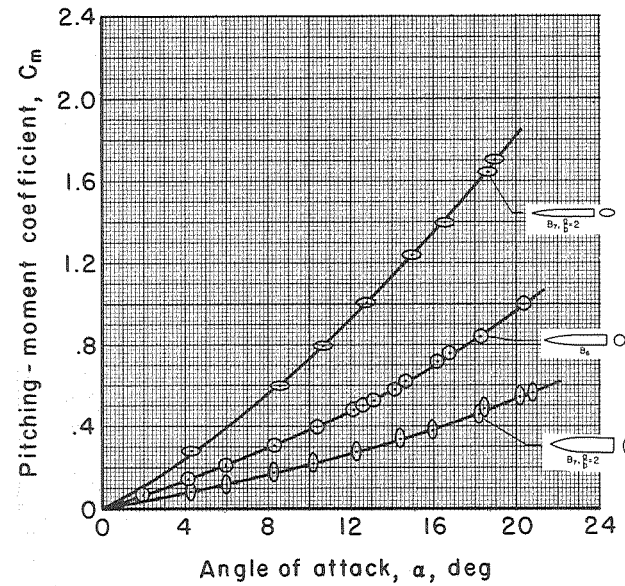


(c) Lift-drag ratio



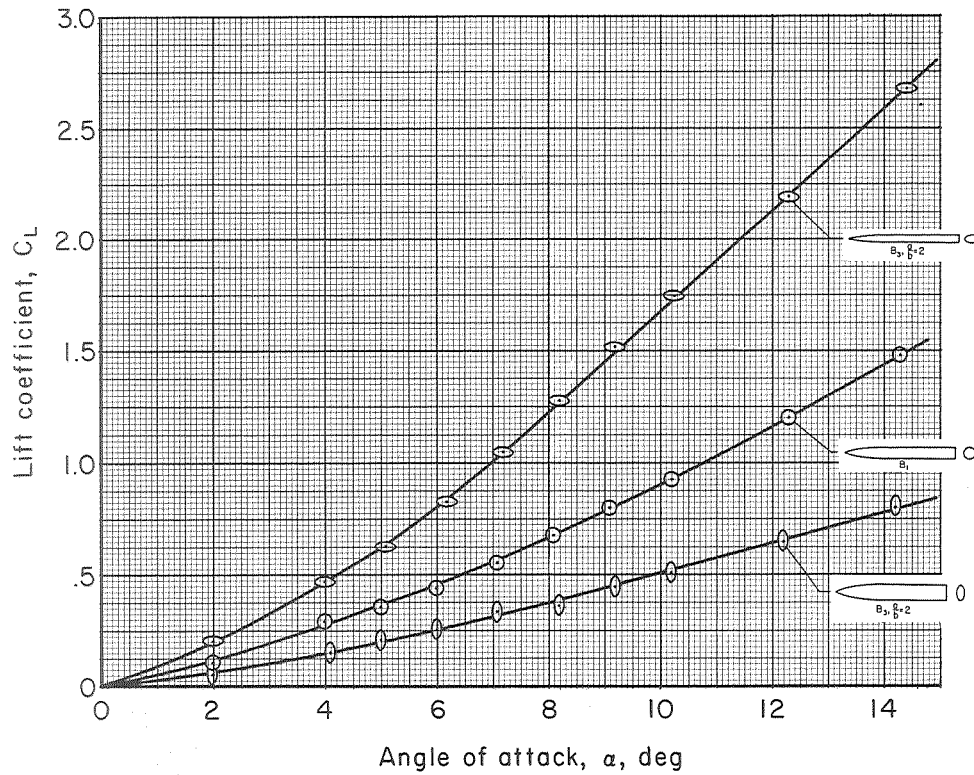
(d) Center of pressure

$$\frac{l}{d} = 6, M_\infty = 1.98, \\ R = 4.0 \times 10^6$$

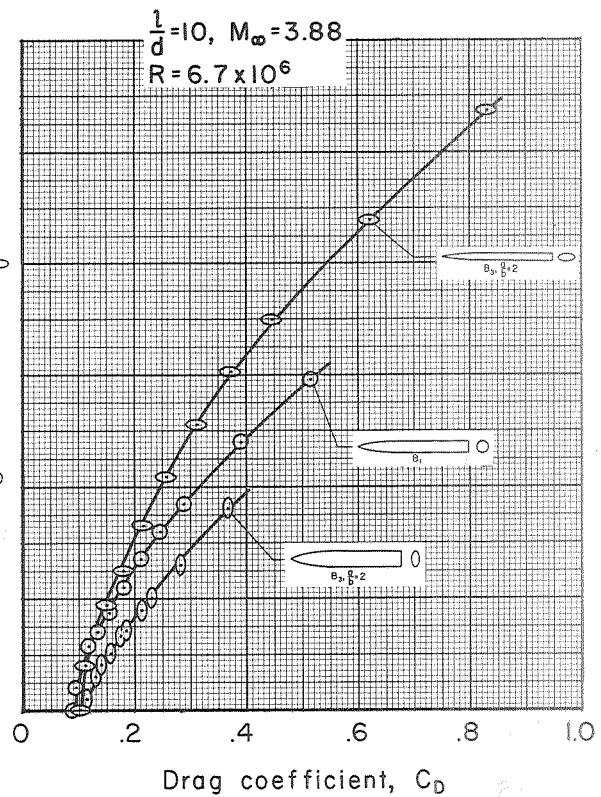


(e) Pitching moment

Figure 4.- Concluded.

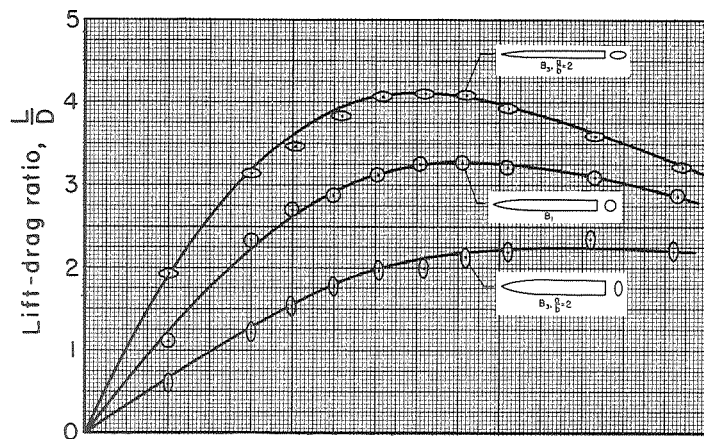


(a) Lift

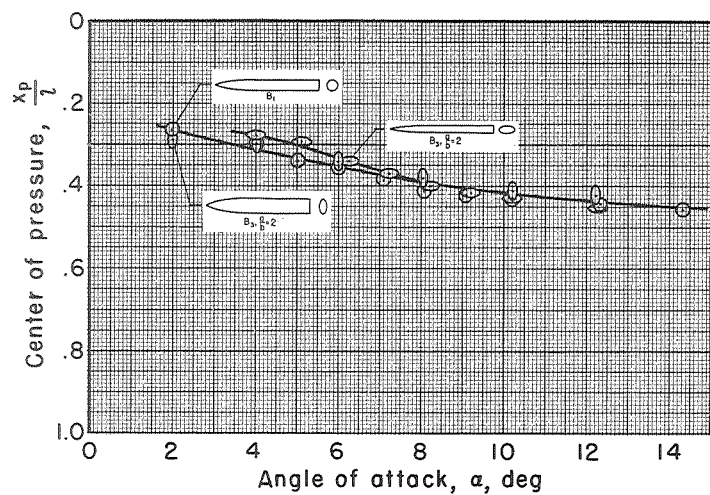


(b) Lift-drag polar

Figure 5.- Effect of change in axis ratio (a/b) on the aerodynamic characteristics for bodies with elliptic cross sections; $l/d = 10$, $M_\infty = 3.88$, $R = 6.7 \times 10^6$.

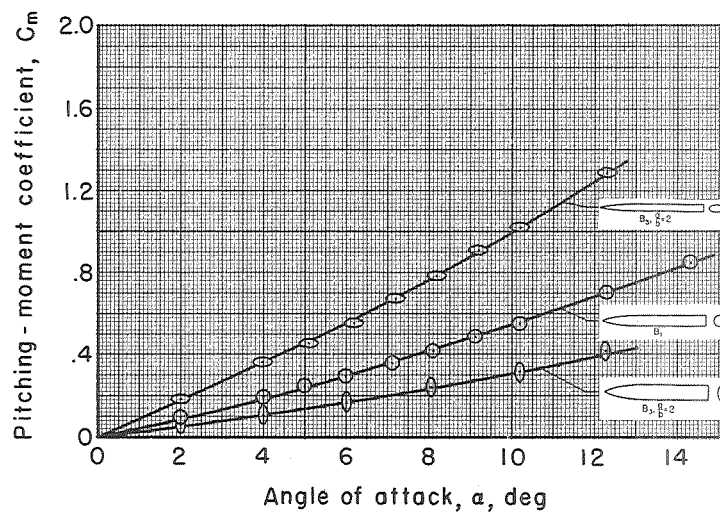


(c) Lift-drag ratio



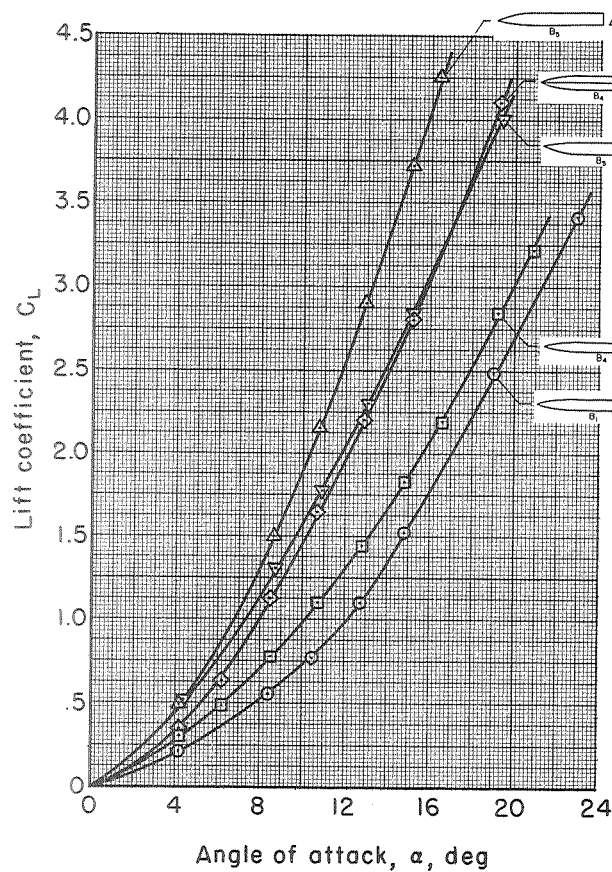
(d) Center of pressure

$$\frac{l}{d}=10, M_{\infty}=3.88, \\ R=6.7 \times 10^6$$

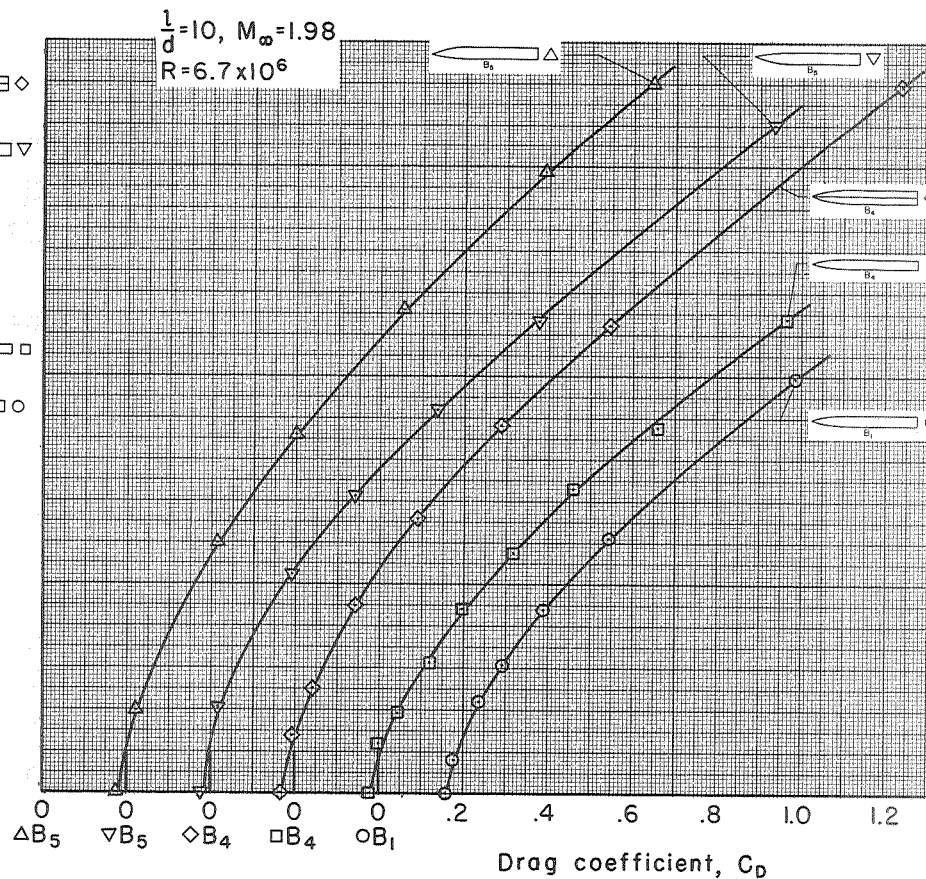


(e) Pitching moment

Figure 5.- Concluded.

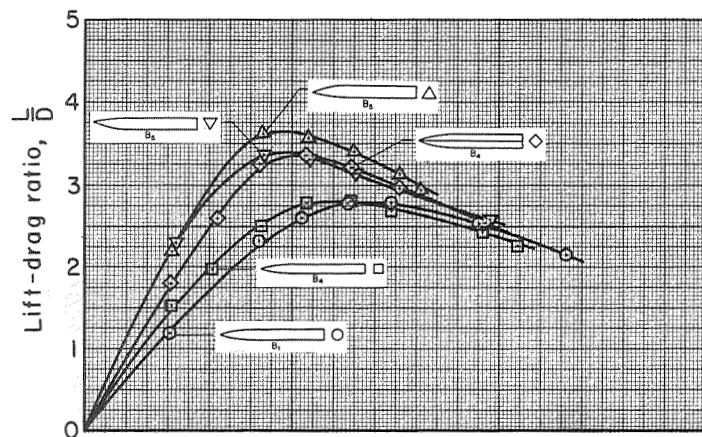


(a) Lift

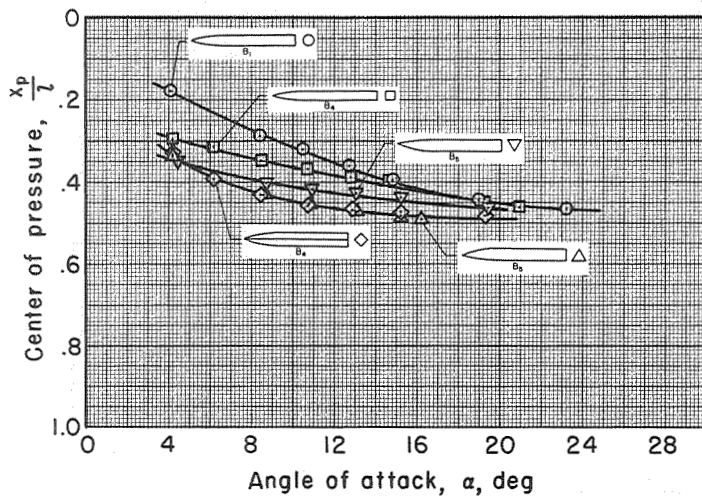


(b) Lift-drag polar

Figure 6.- Comparisons of aerodynamic characteristics for bodies with circular, square, and triangular cross sections; $l/d = 10$, $M_\infty = 1.98$, $R = 6.7 \times 10^6$.

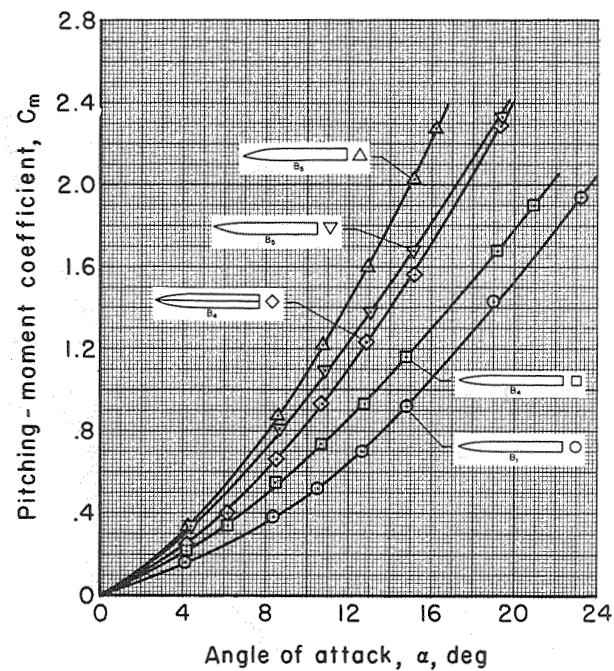


(c) Lift-drag ratio



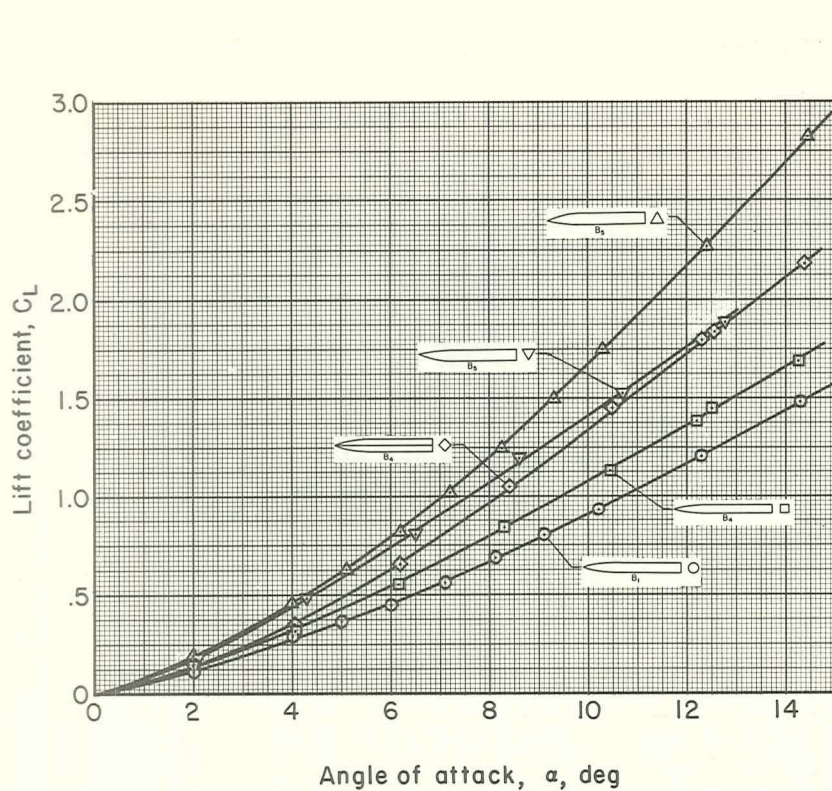
(d) Center of pressure

$\frac{l}{d}=10, M_\infty=1.98,$
 $R=6.7 \times 10^6$

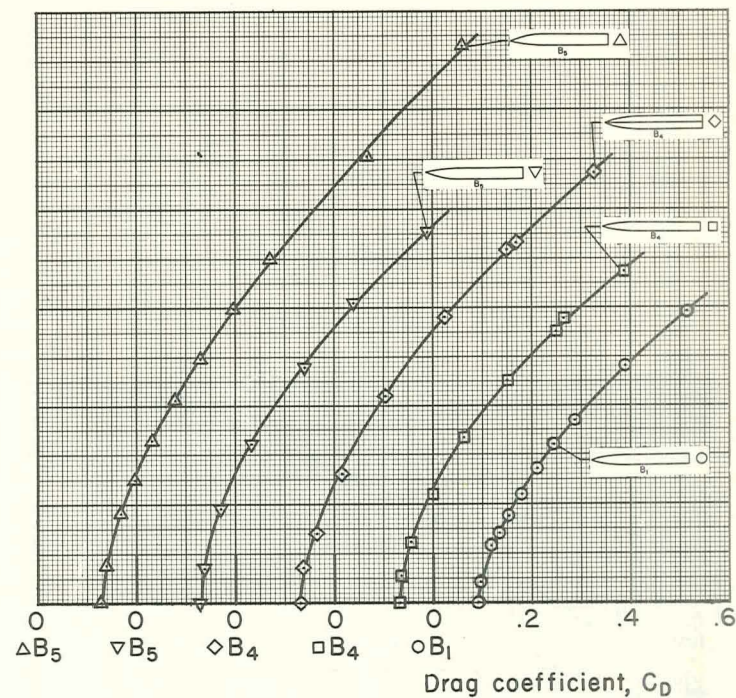


(e) Pitching moment

Figure 6.- Concluded.

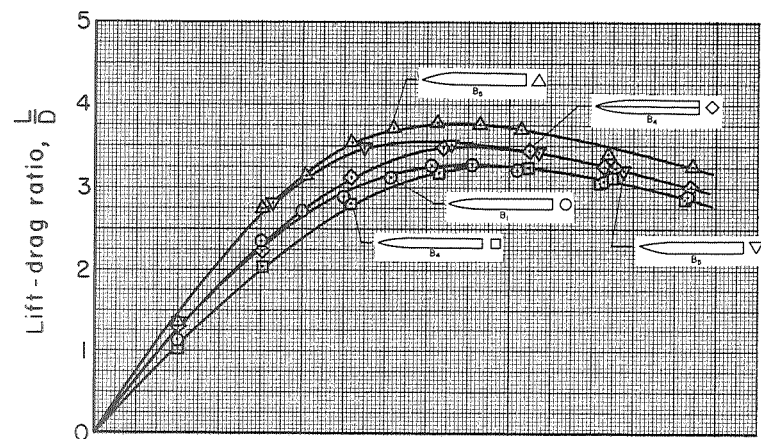


(a) Lift

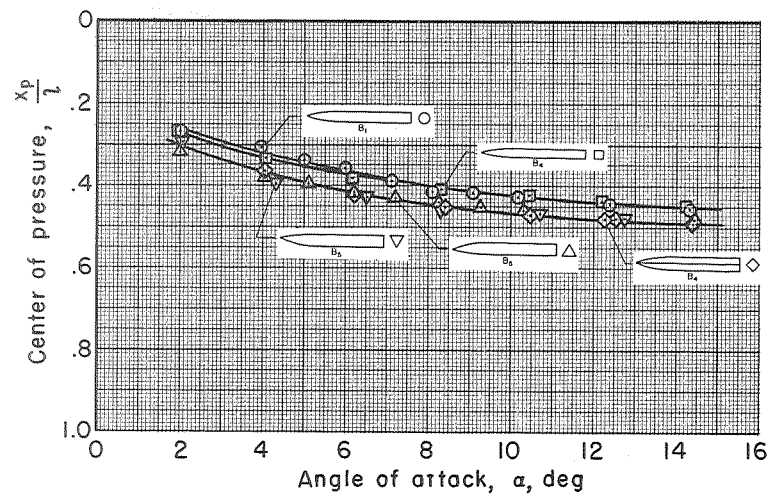


(b) Lift-drag polar

Figure 7.- Comparisons of aerodynamic characteristics for bodies with circular, square, and triangular cross sections; $l/d = 10$, $M_\infty = 3.88$, $R = 6.7 \times 10^6$.

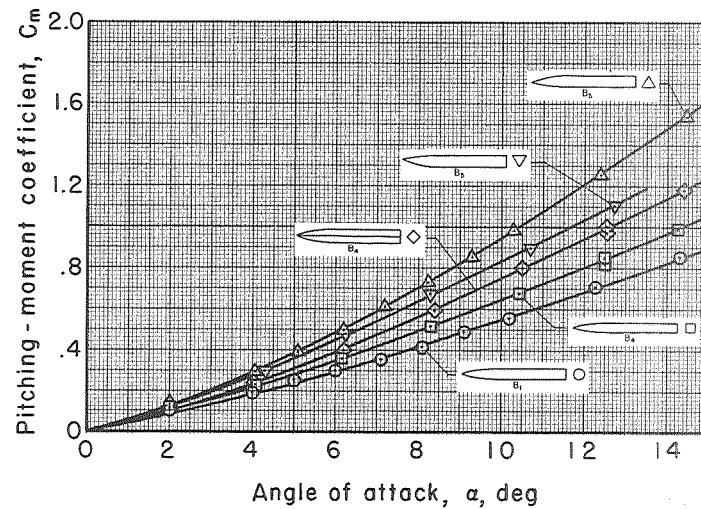


(c) Lift-drag ratio



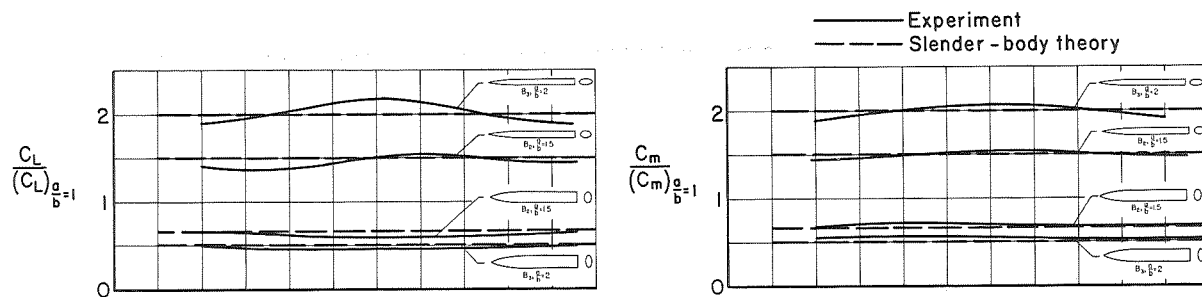
(d) Center of pressure

$$\frac{l}{d}=10, M_{\infty}=3.88, \\ R=6.7 \times 10^6$$

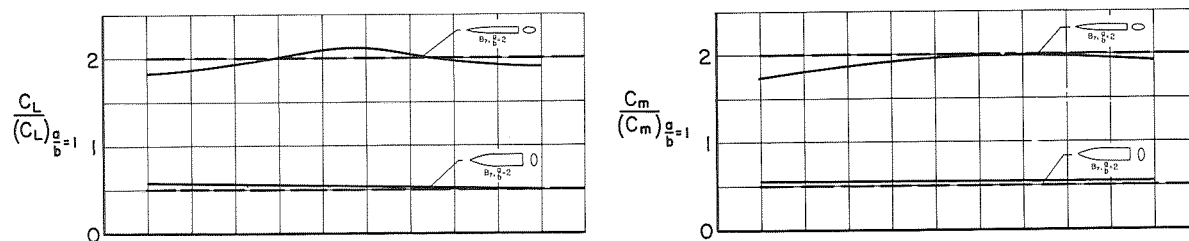


(e) Pitching moment

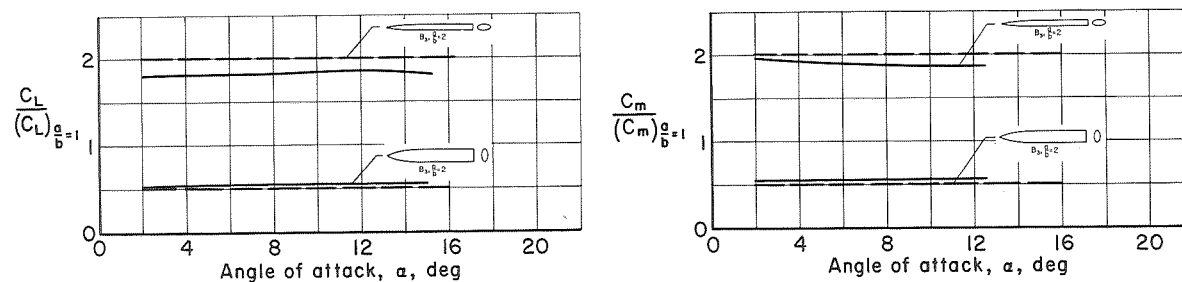
Figure 7.- Concluded.



(a) $l/d = 10$; $M_\infty = 1.98$; $R = 6.7 \times 10^6$

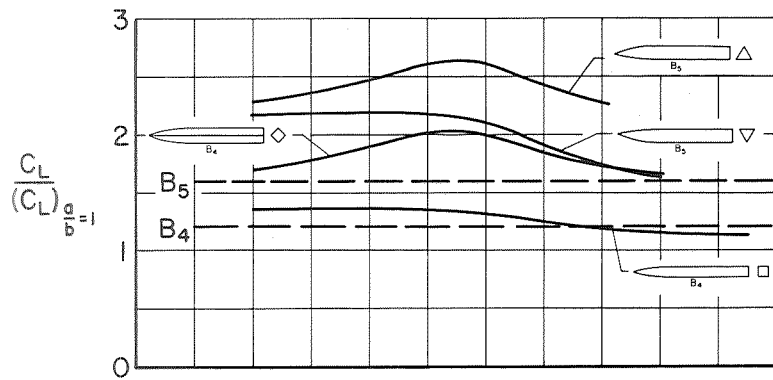


(b) $l/d = 6$; $M_\infty = 1.98$; $R = 4.0 \times 10^6$

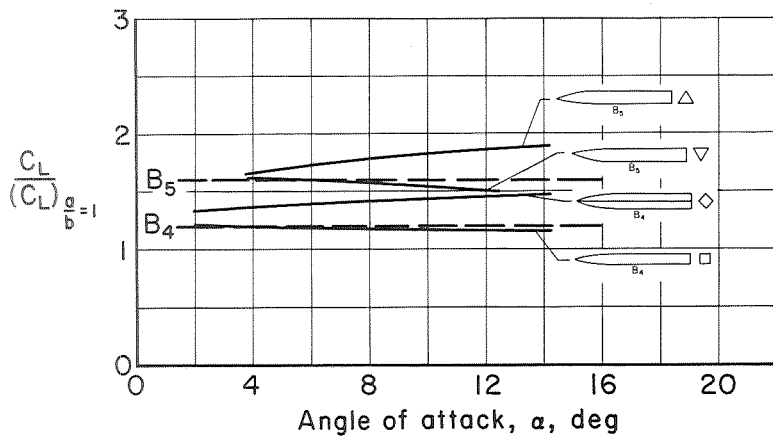


(c) $l/d = 10$; $M_\infty = 3.88$; $R = 6.7 \times 10^6$

Figure 8.- Correlation of lift and pitching-moment data for bodies with elliptic cross sections.



(a) $l/d = 10$; $M_\infty = 1.98$; $R = 6.7 \times 10^6$



(b) $l/d = 10$; $M_\infty = 3.88$; $R = 6.7 \times 10^6$

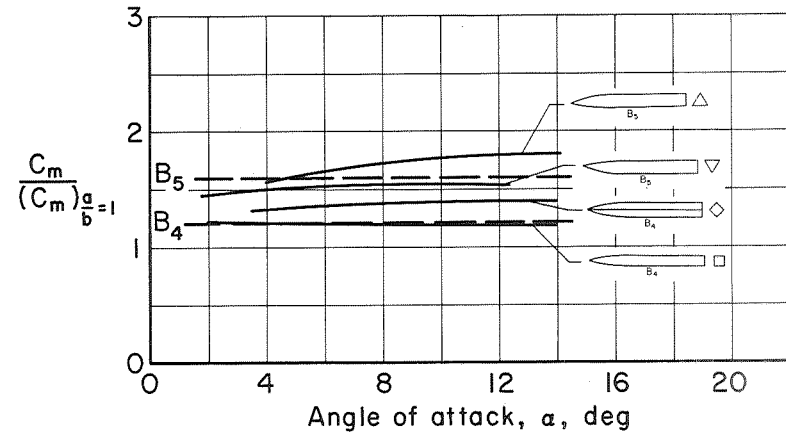
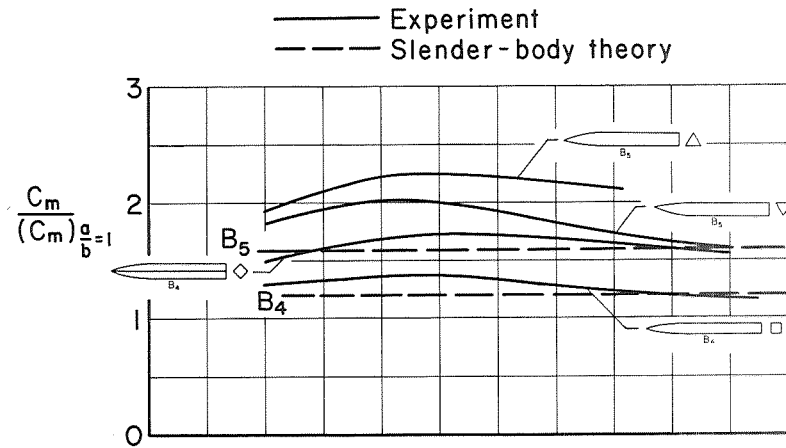


Figure 9.- Correlation of lift and pitching-moment data for bodies with square and triangular cross sections.

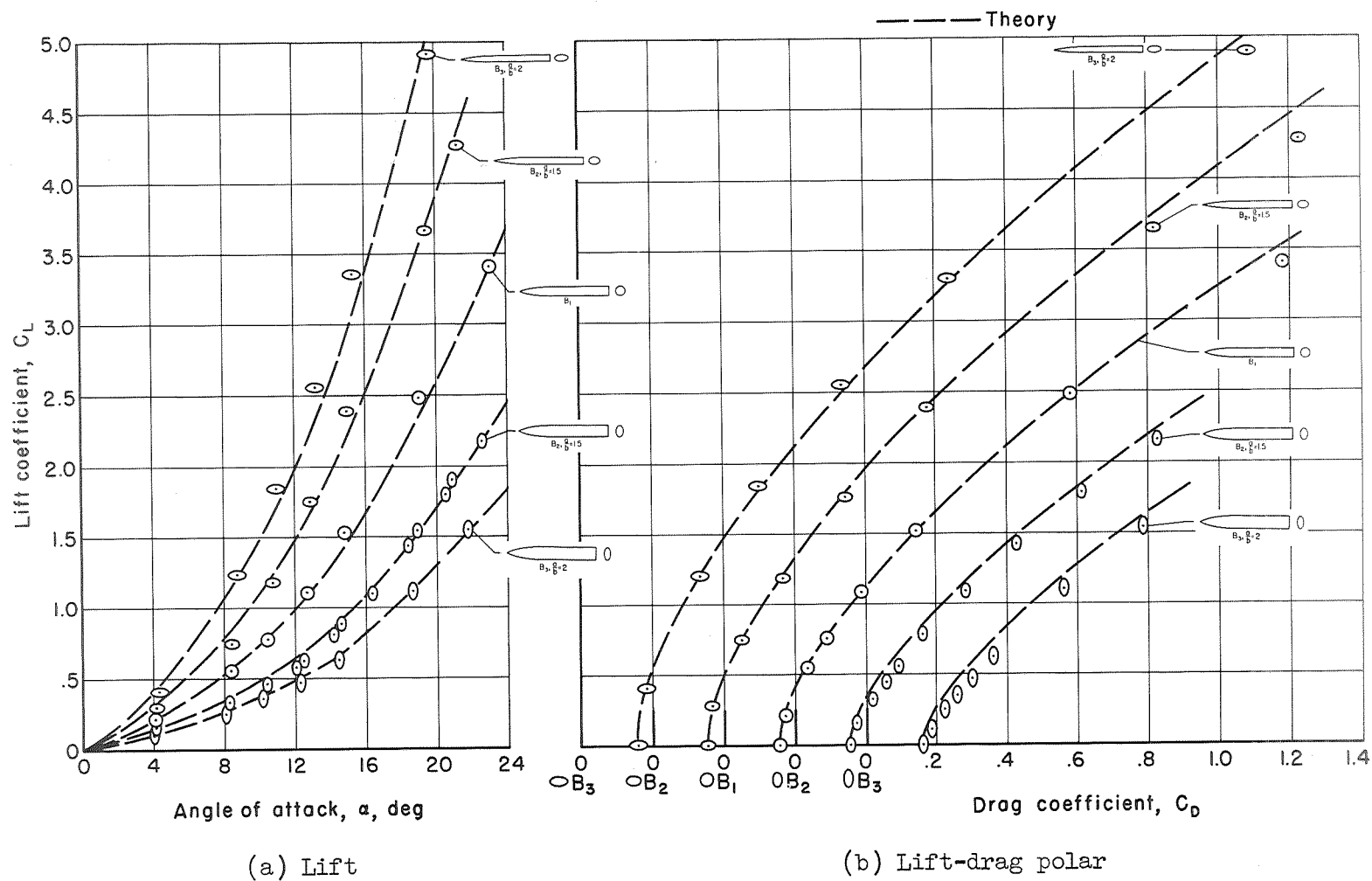
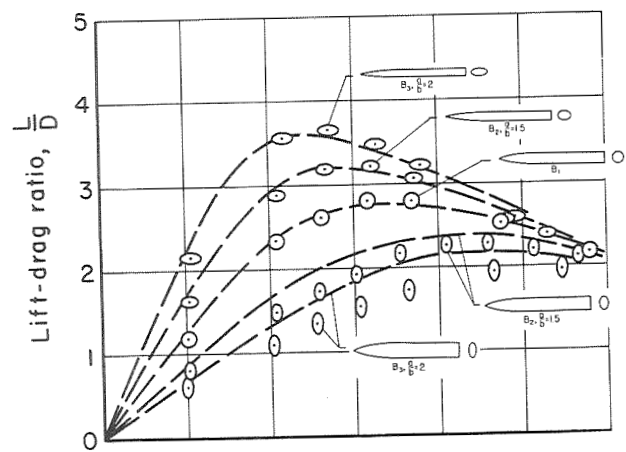
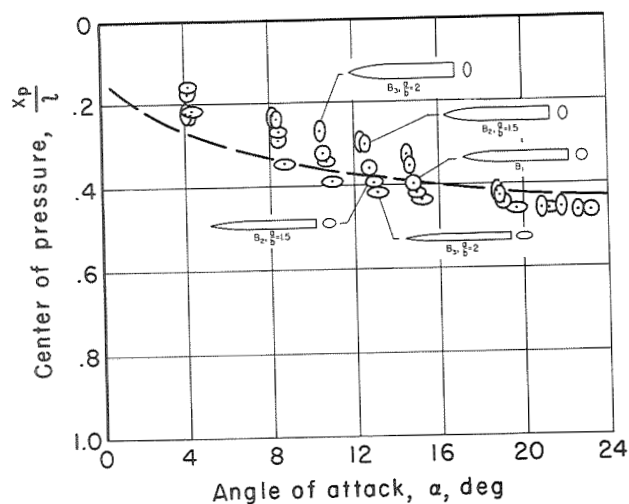


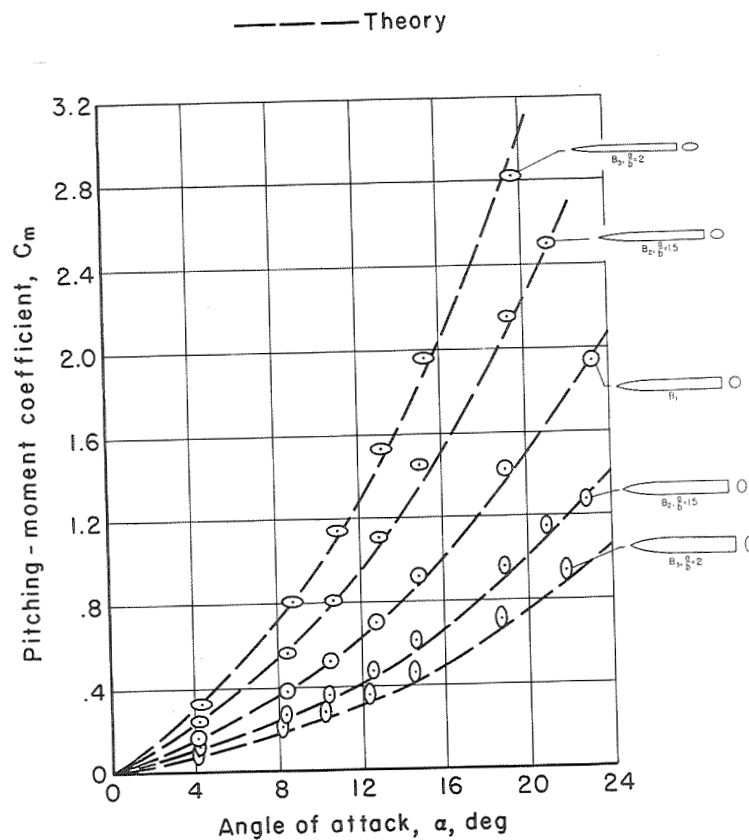
Figure 10.- Comparisons of theoretical and experimental aerodynamic characteristics for bodies with elliptic cross sections; $l/d = 10$, $M_\infty = 1.98$, $R = 6.7 \times 10^6$.



(c) Lift-drag ratio

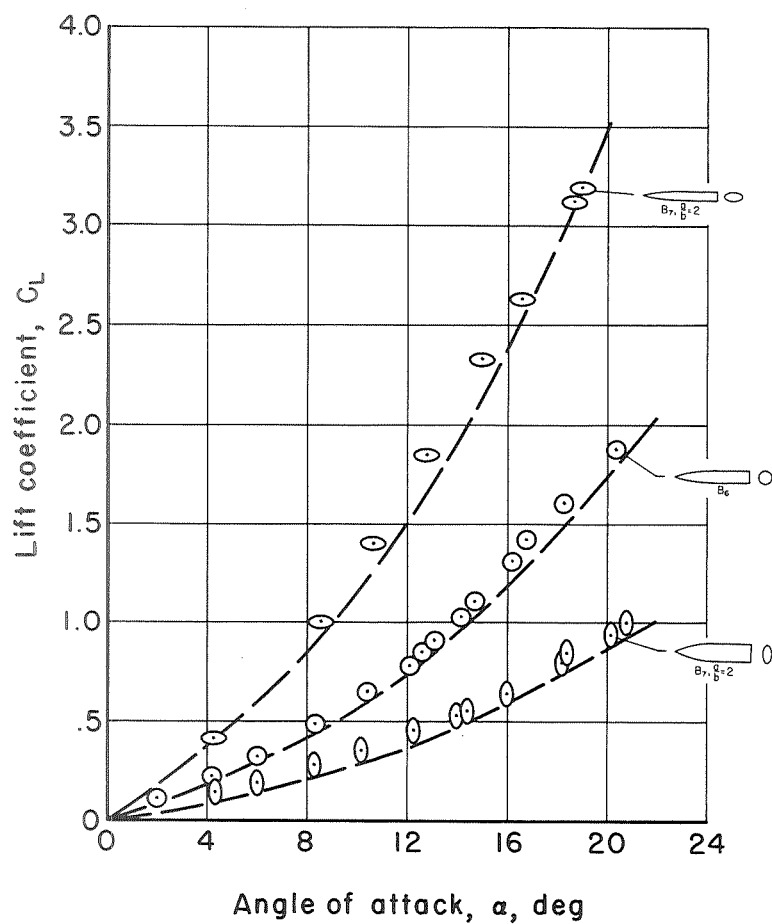


(d) Center of pressure

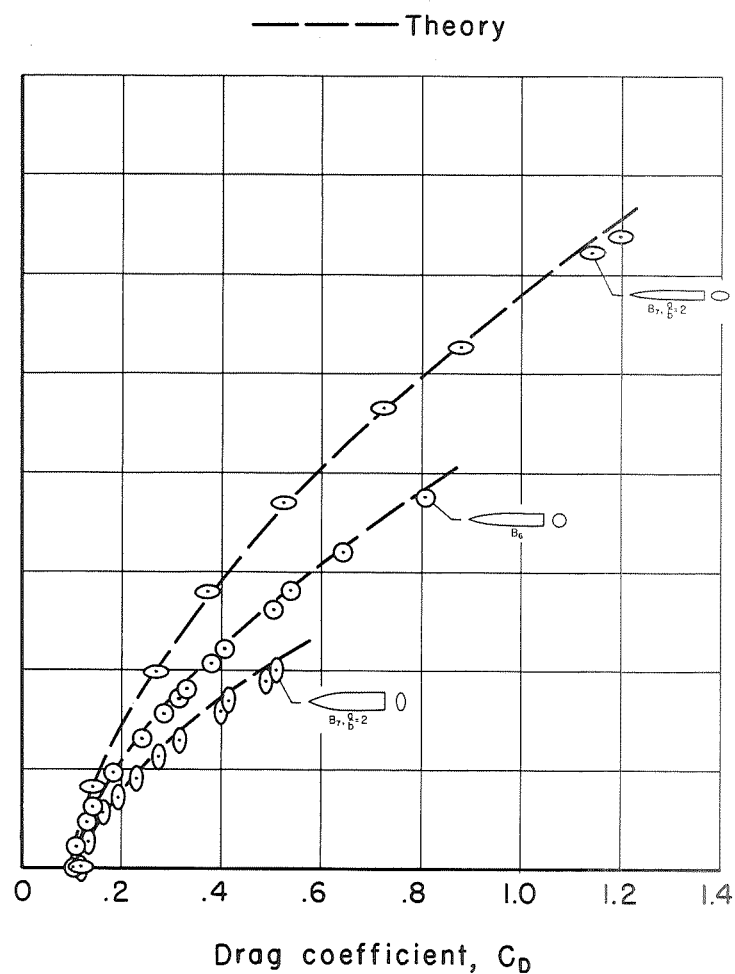


(e) Pitching moment

Figure 10.- Concluded.

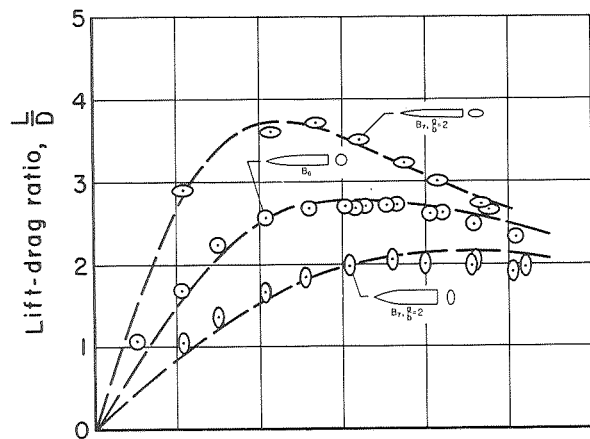


(a) Lift

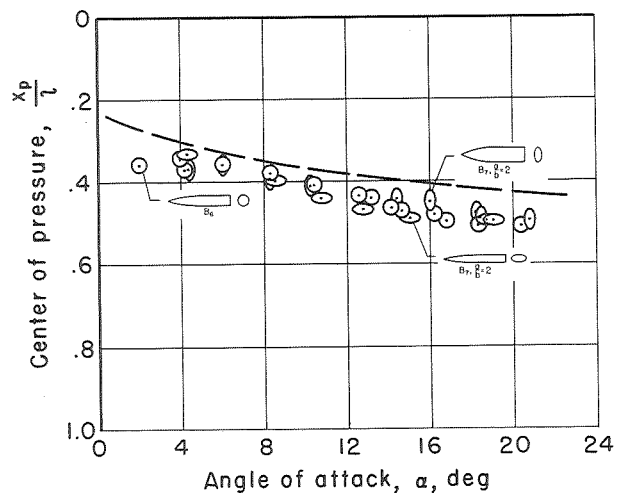


(b) Lift-drag polar

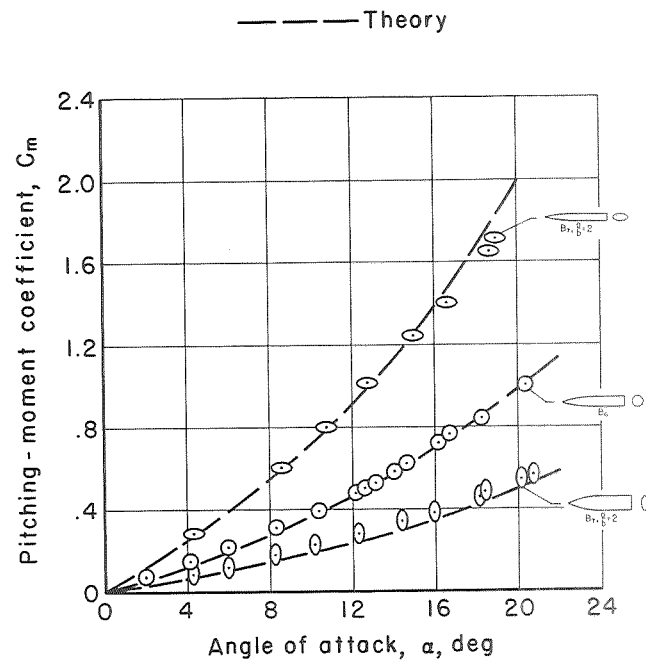
Figure 11.- Comparisons of theoretical and experimental aerodynamic characteristics for bodies with elliptic cross sections; $l/d = 6$, $M_\infty = 1.98$, $R = 4.0 \times 10^6$.



(c) Lift-drag ratio

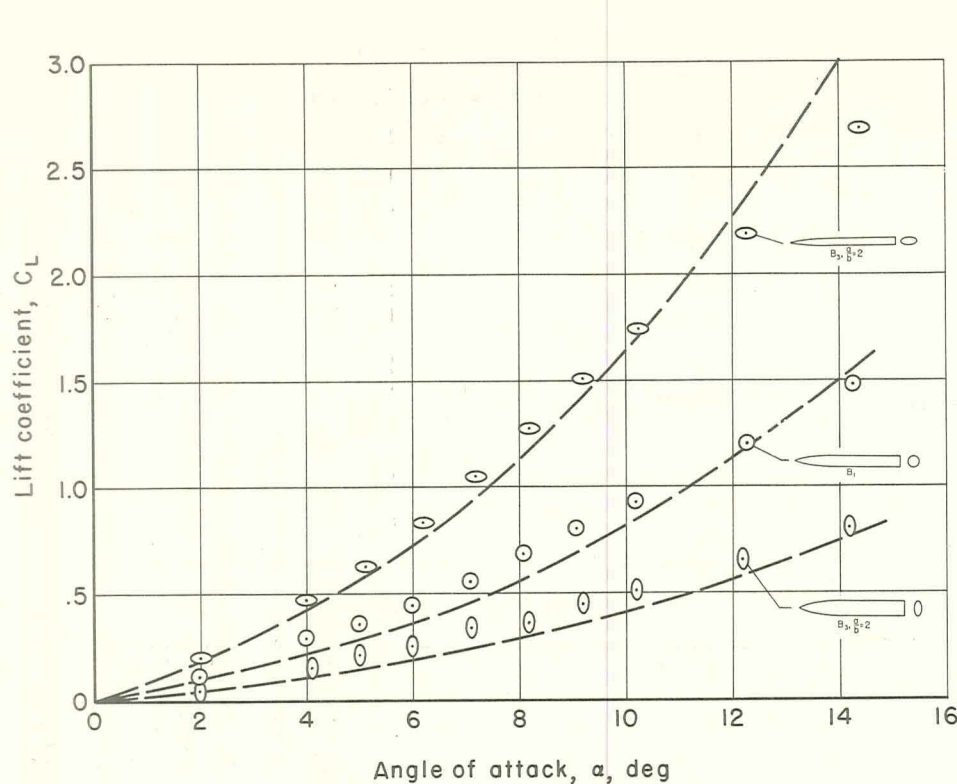


(d) Center of pressure

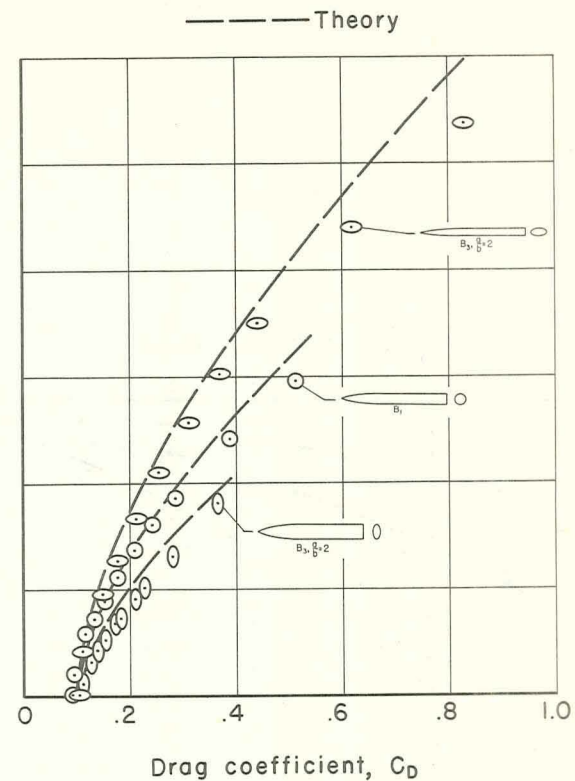


(e) Pitching moment

Figure 11.- Concluded.

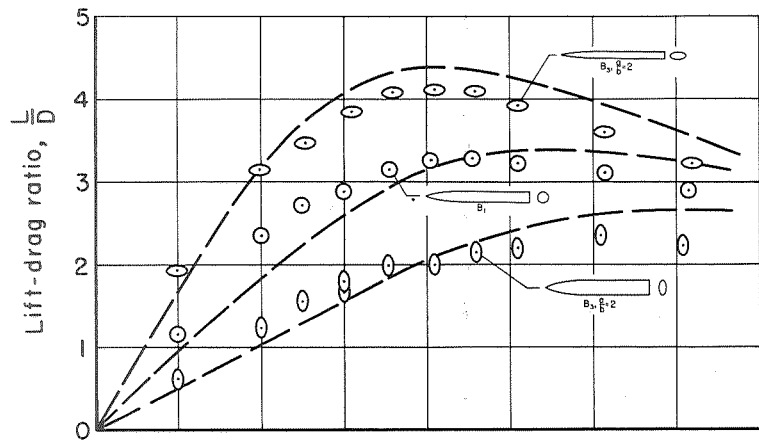


(a) Lift

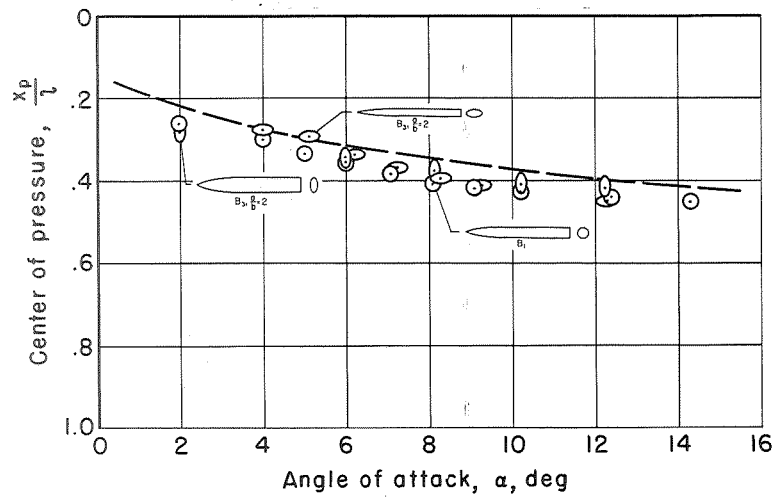


(b) Lift-drag polar

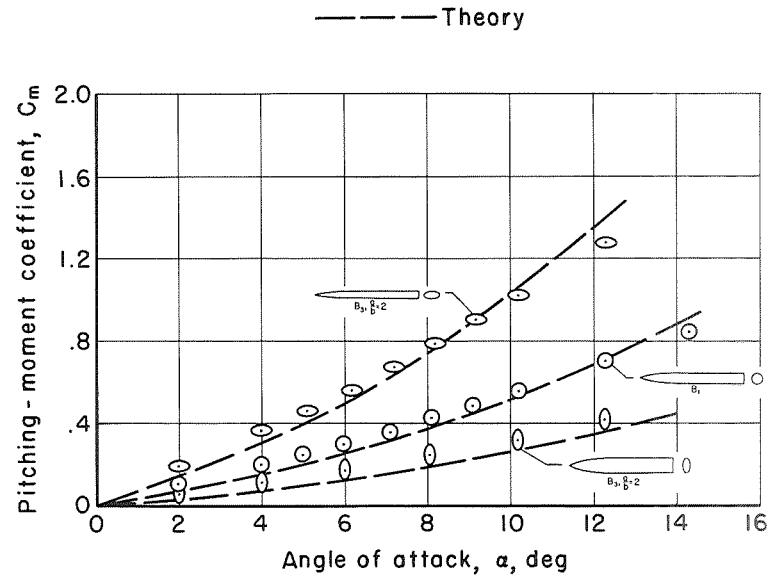
Figure 12.- Comparisons of theoretical and experimental aerodynamic characteristics for bodies with elliptic cross sections; $l/d = 10$, $M_\infty = 3.88$, $R = 6.7 \times 10^6$.



(c) Lift-drag ratio

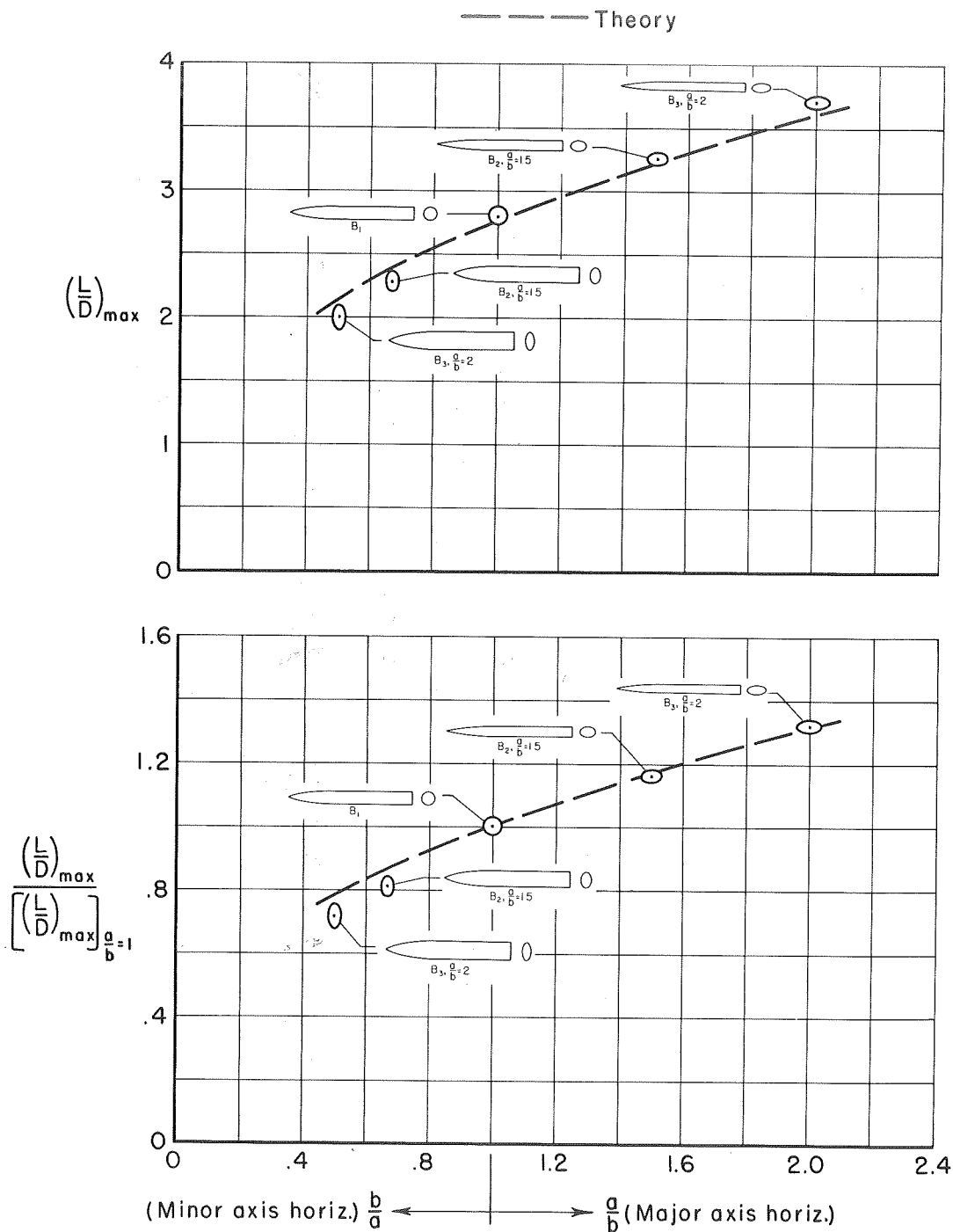


(d) Center of pressure



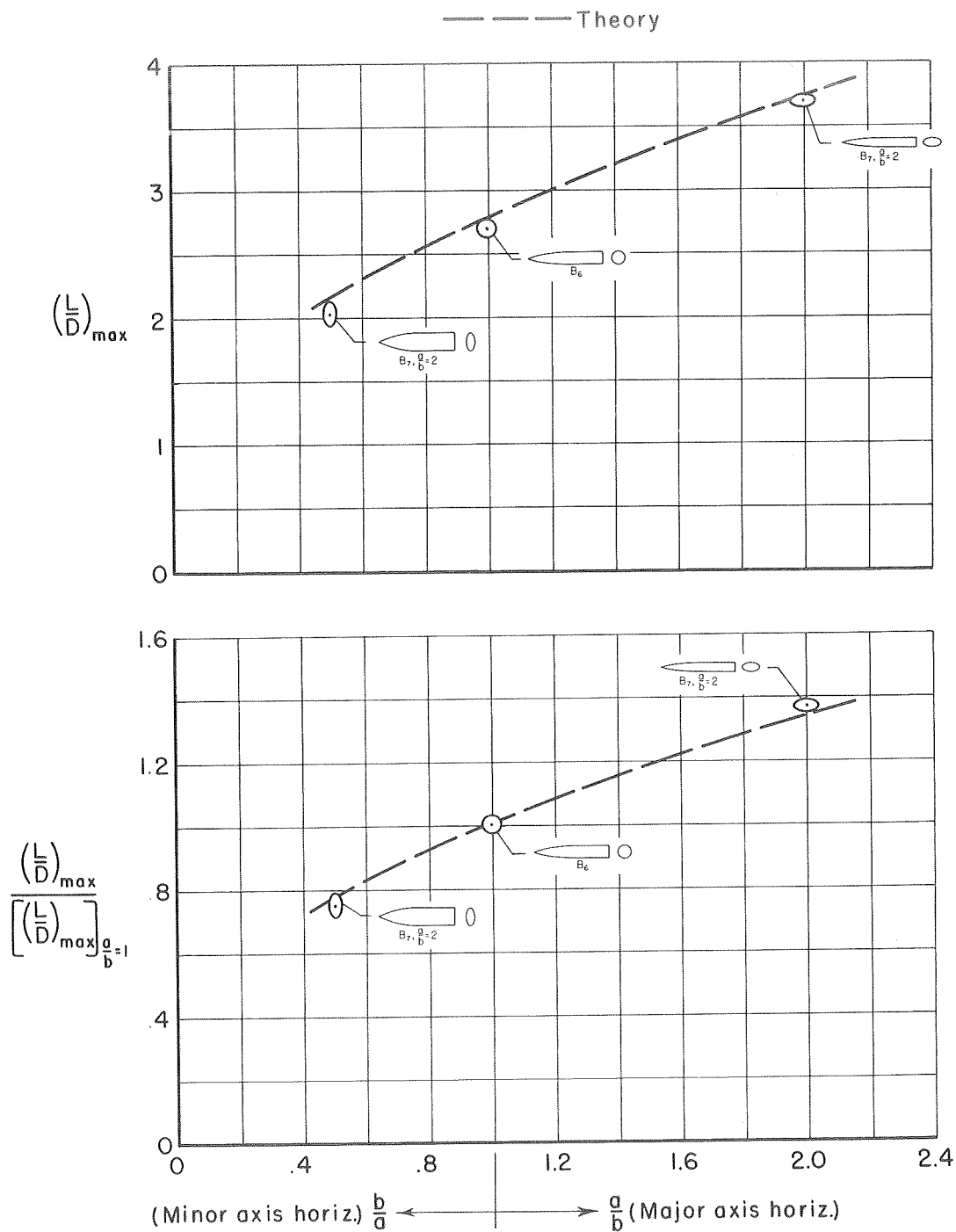
(e) Pitching moment

Figure 12.- Concluded.



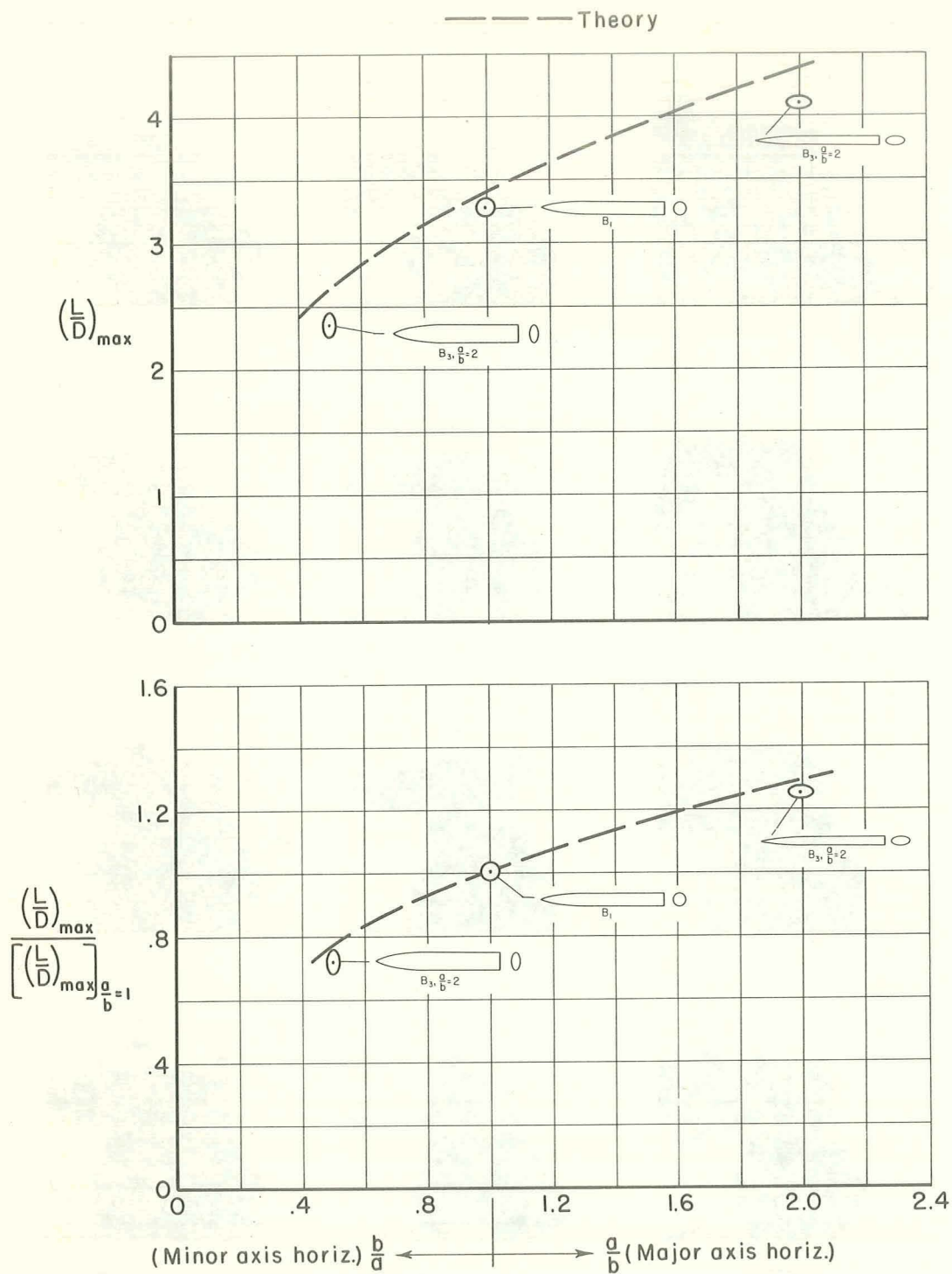
(a) $l/d = 10$, $M_{\infty} = 1.98$, $R = 6.7 \times 10^6$

Figure 13.- Comparisons of theoretical and experimental maximum lift-drag ratios for bodies with elliptic cross sections.



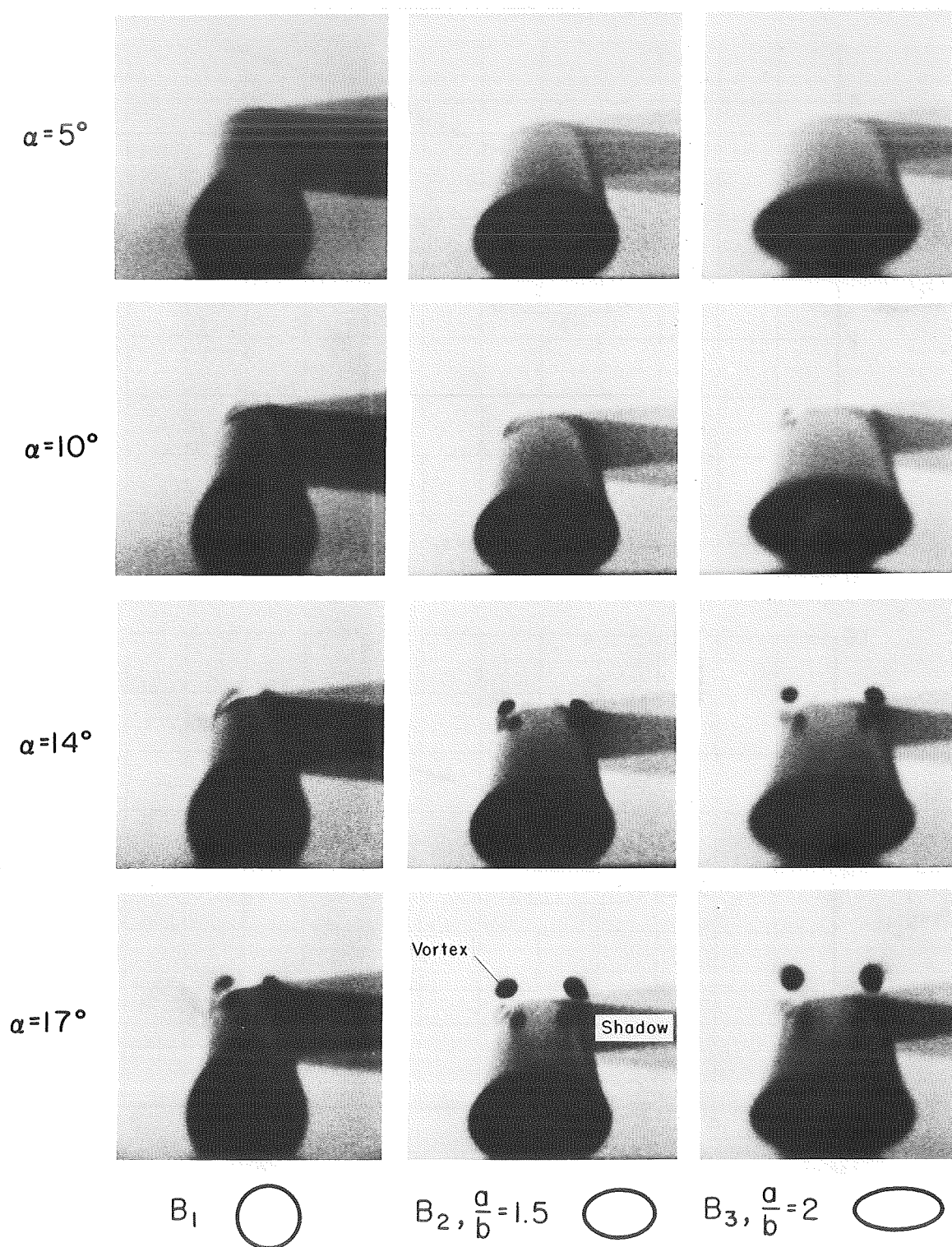
(b) $l/d = 6$, $M_{\infty} = 1.98$, $R = 4.0 \times 10^6$

Figure 13.- Continued.



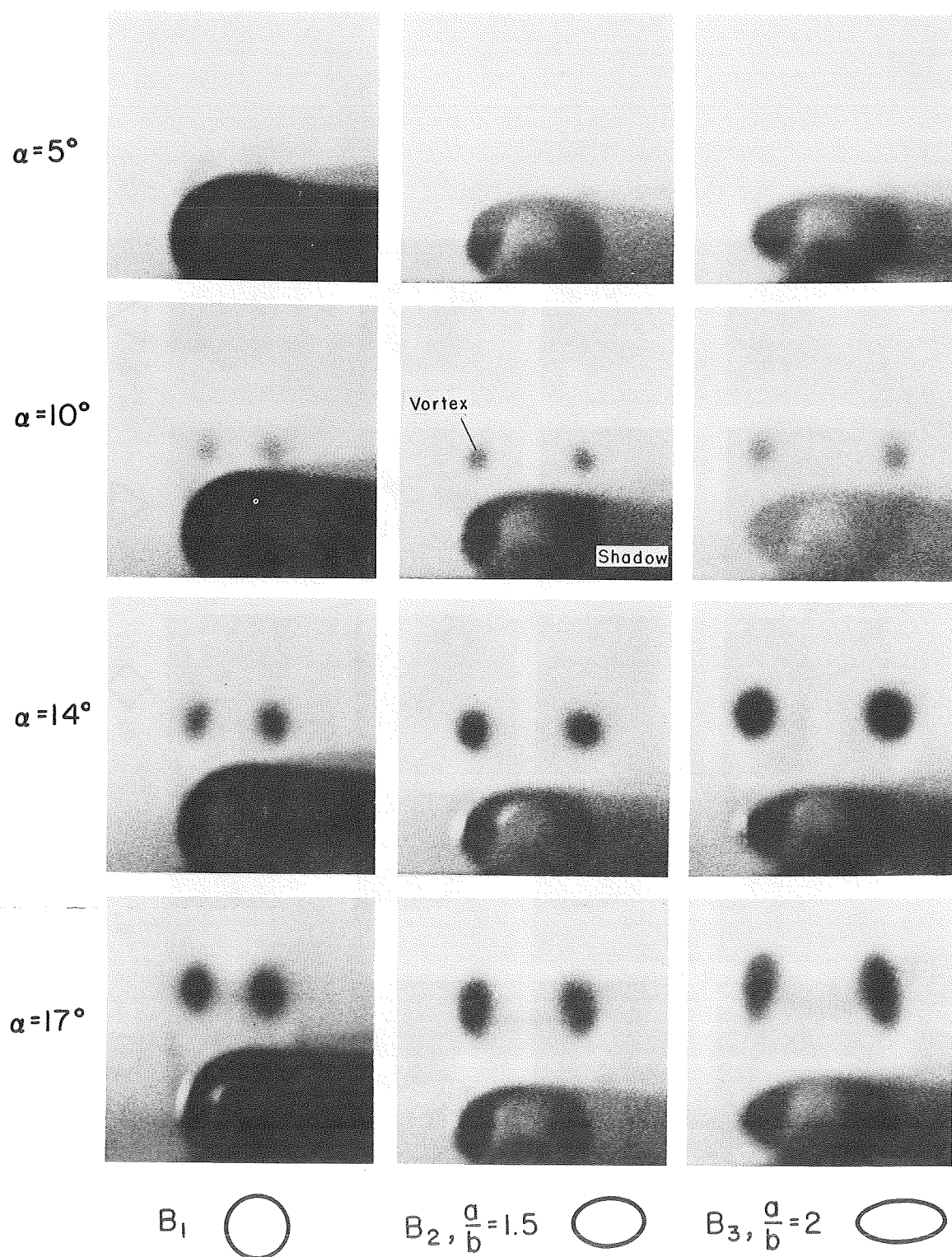
(c) $l/d = 10$, $M_{\infty} = 3.88$, $R = 6.7 \times 10^6$

Figure 13.- Concluded.

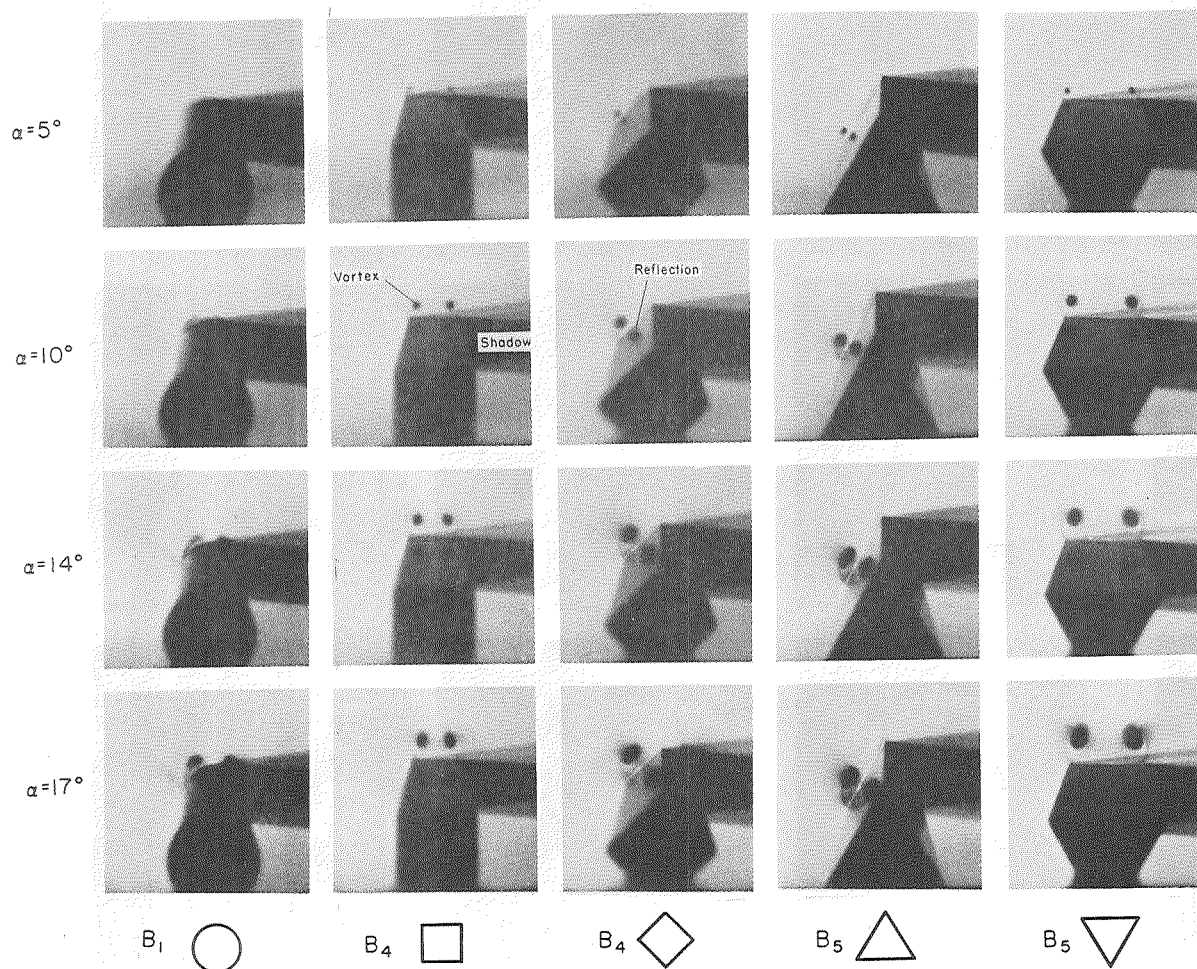


(a) Vapor-screen light plane at $x = 5d$.

Figure 14.- Rear views of elliptic bodies showing effect of axis ratio a/b and angle of attack on vortex patterns; $M_\infty = 1.98$, $R = 6.7 \times 10^6$.

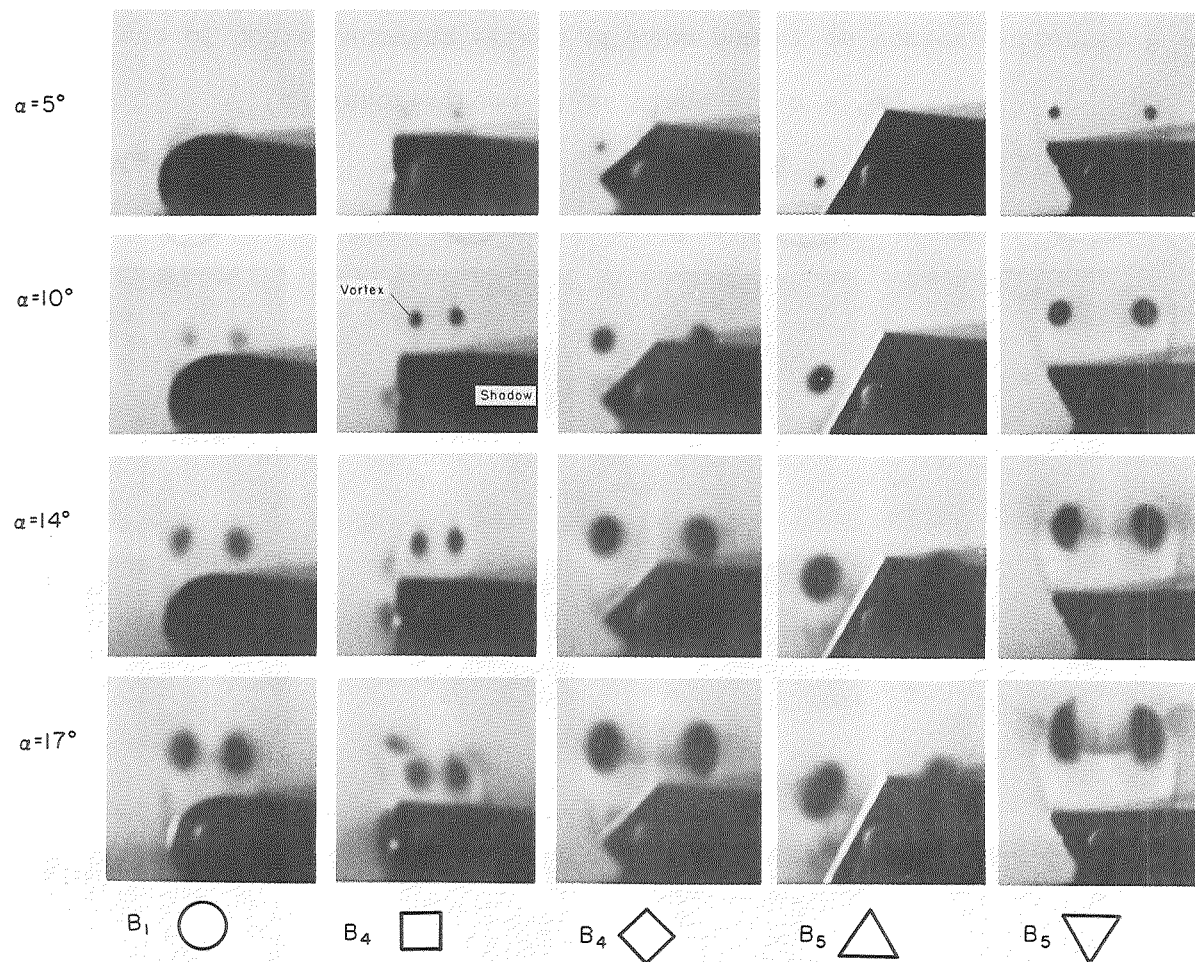


(b) Vapor-screen light plane at $x = 10d$ (body base).



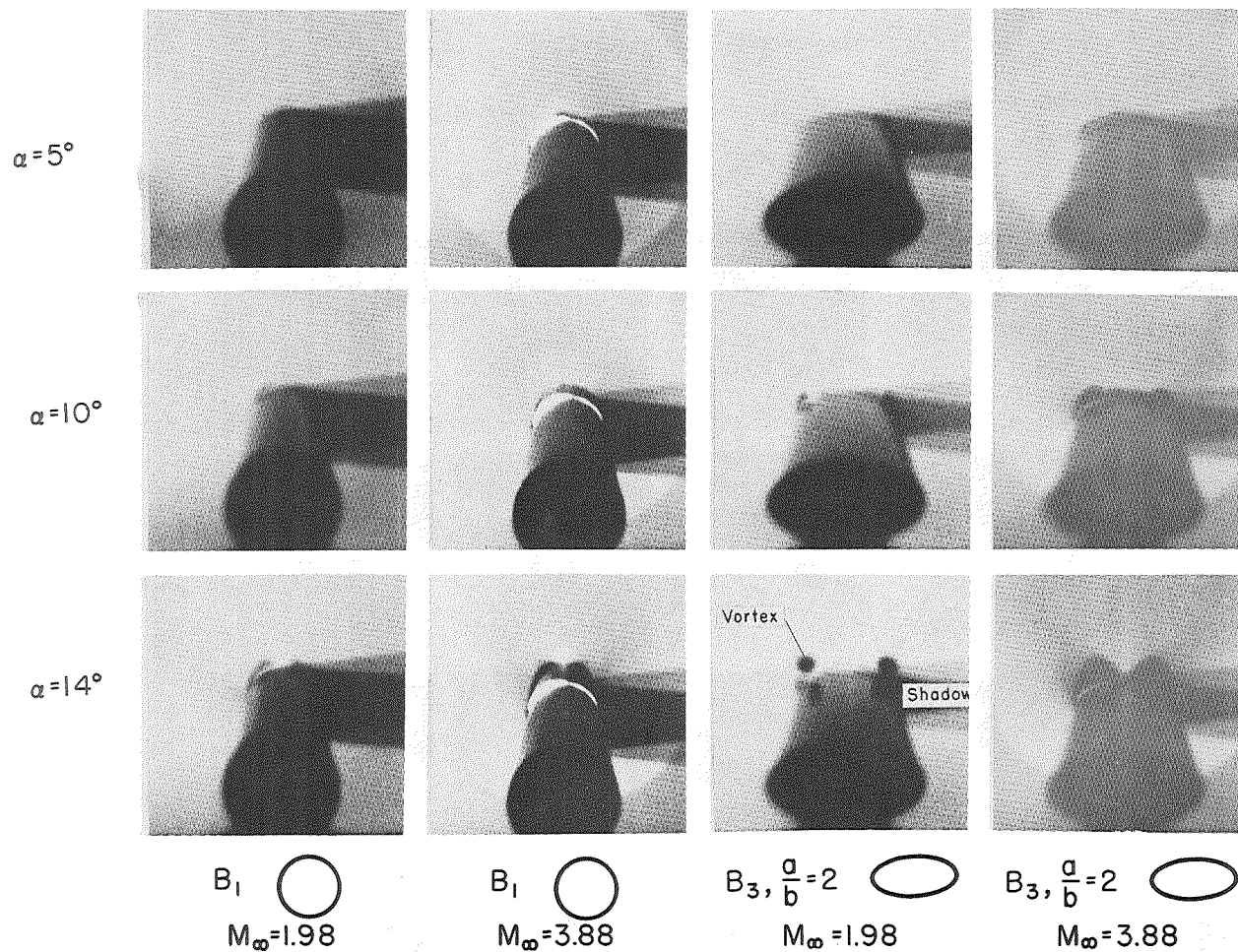
(a) Vapor-screen light plane at $x = 5d$.

Figure 15.- Rear views of bodies showing effect of cross section (circular, square, and triangular) and angle of attack on vortex patterns; $M_\infty = 1.98$, $R = 6.7 \times 10^6$.



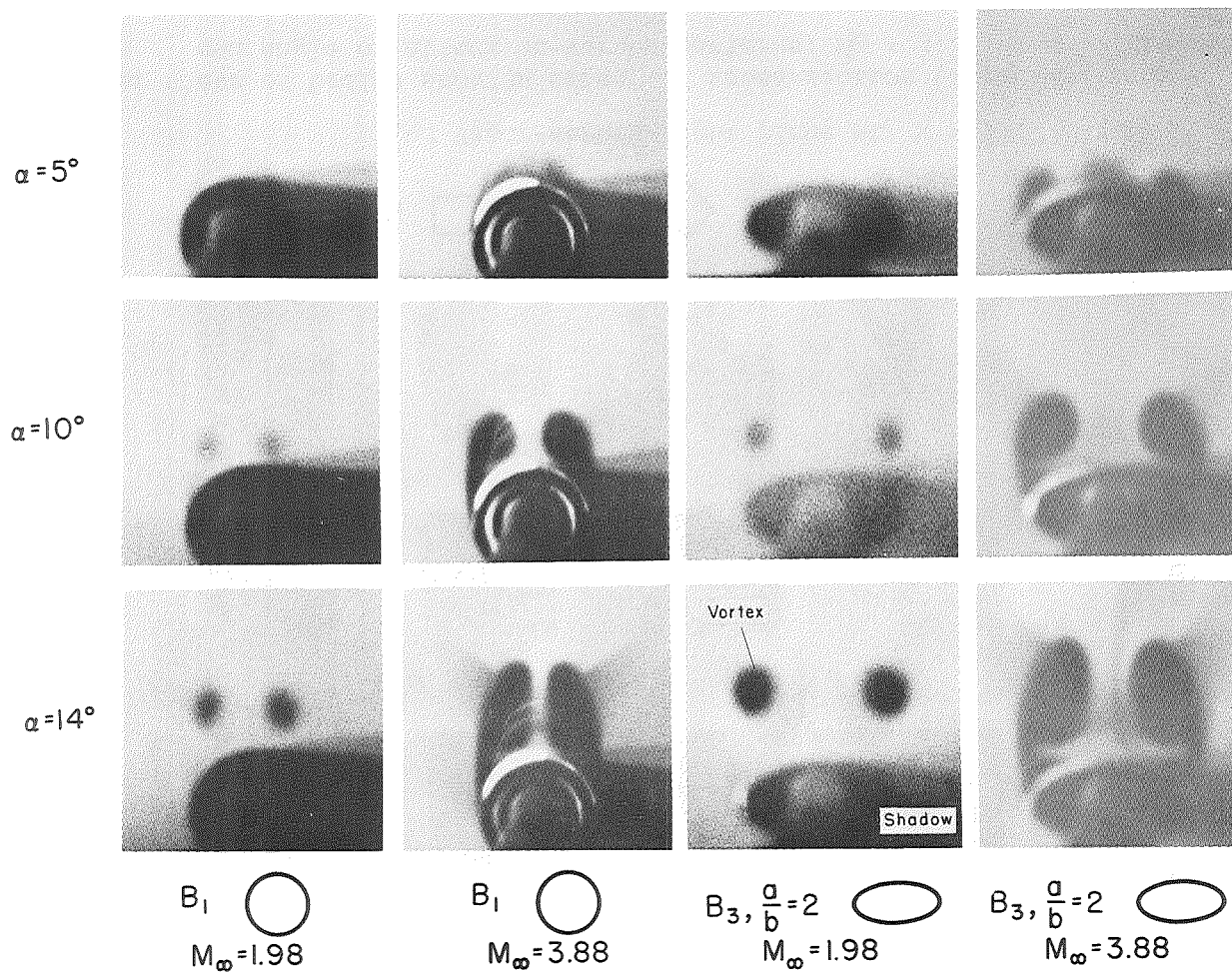
(b) Vapor-screen light plane at $x = 10d$ (body base).

Figure 15.- Concluded.



(a) Vapor-screen light plane at $x = 5d$.

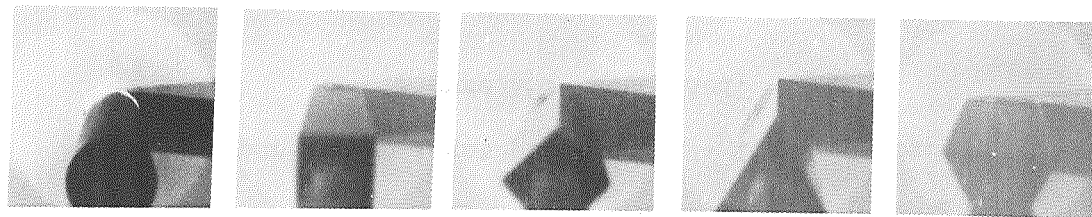
Figure 16.- Rear views of bodies showing effect of Mach number on vortex patterns; $R = 6.7 \times 10^6$.



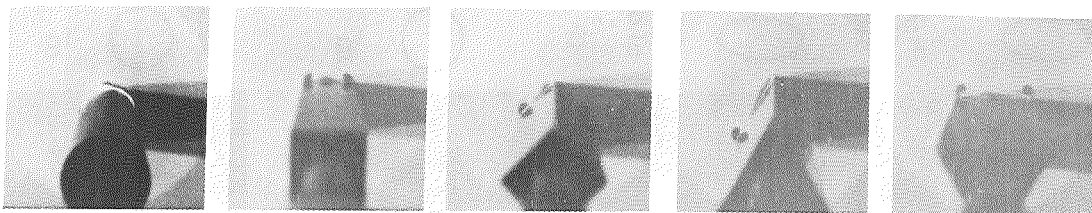
(b) Vapor-screen light plane at $x = 10d$ (body base).

Figure 16.- Concluded.

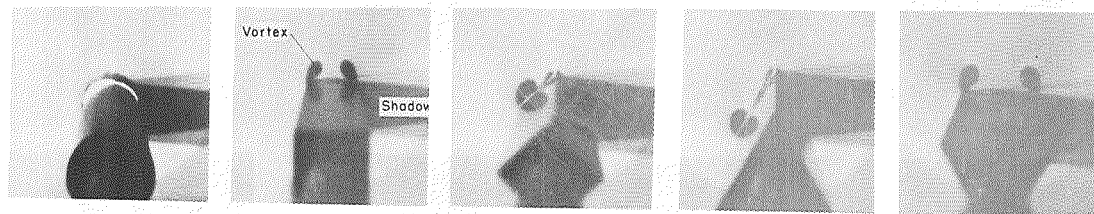
$\alpha = 0^\circ$



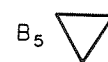
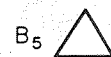
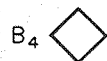
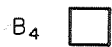
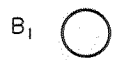
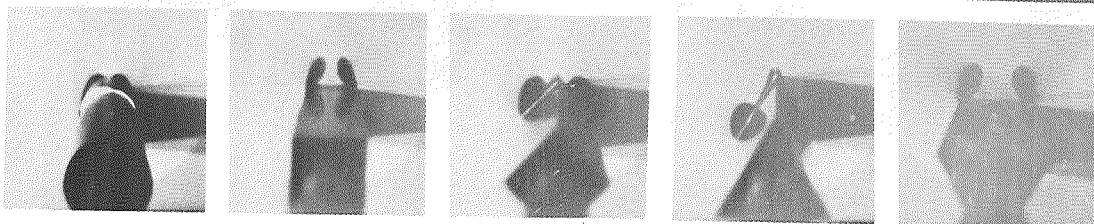
$\alpha = 5^\circ$



$\alpha = 10^\circ$

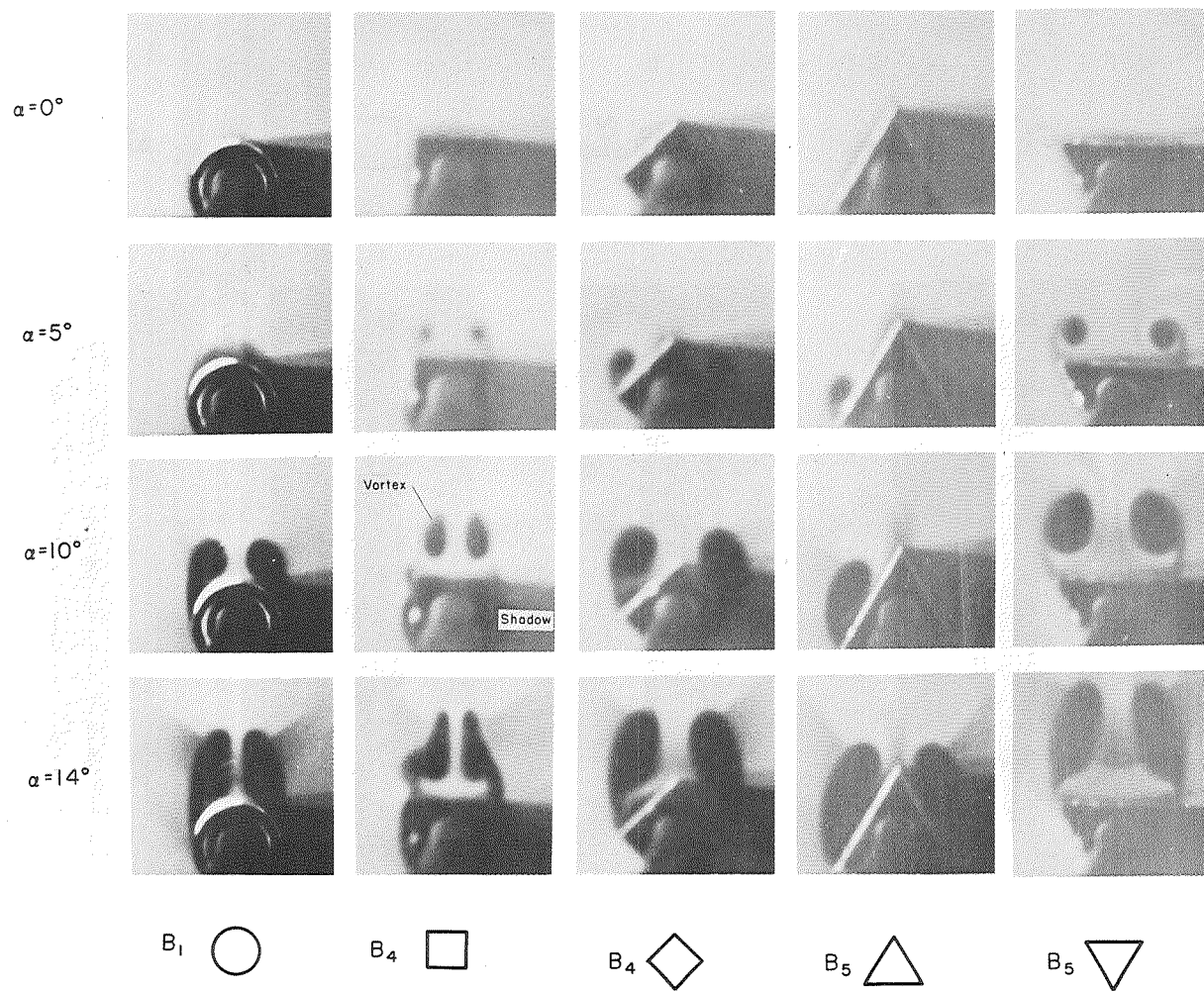


$\alpha = 14^\circ$



(a) Vapor-screen light plane at $x = 5d$.

Figure 17.- Rear views of bodies showing effect of cross section (circular, square, and triangular) and angle of attack on vortex patterns; $M_\infty = 3.88$, $R = 6.7 \times 10^6$.



(b) Vapor-screen light plane at $x = 10d$ (body base).

Figure 17.- Concluded.

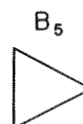
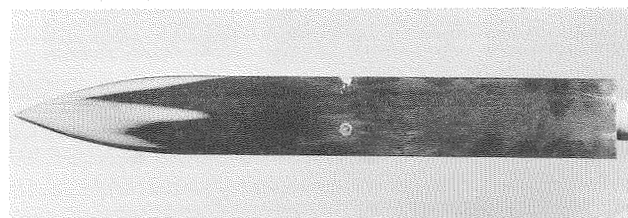
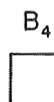
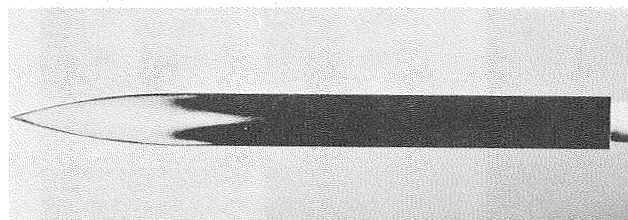
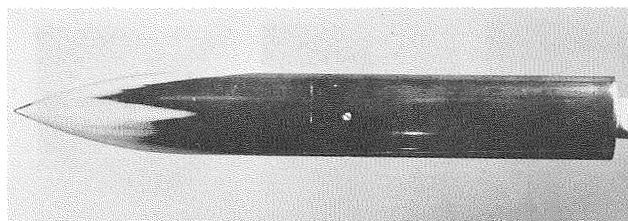
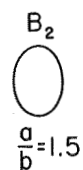
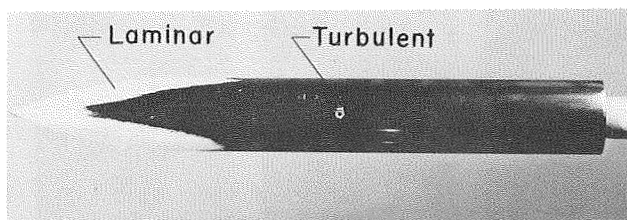
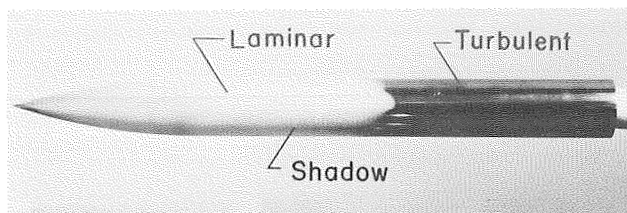
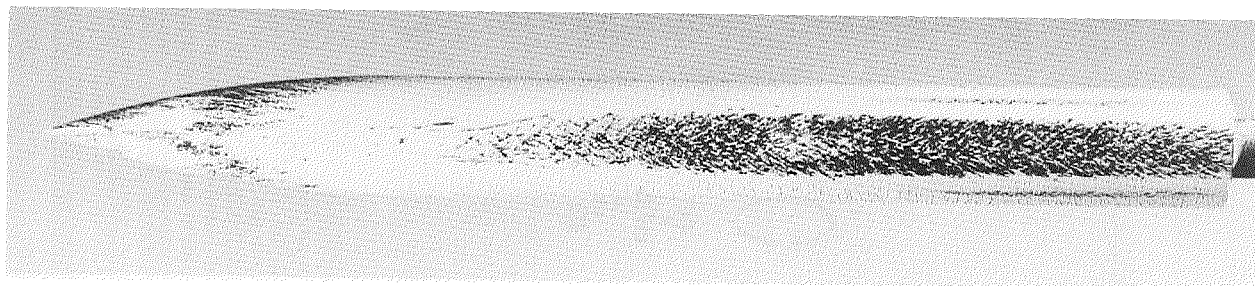
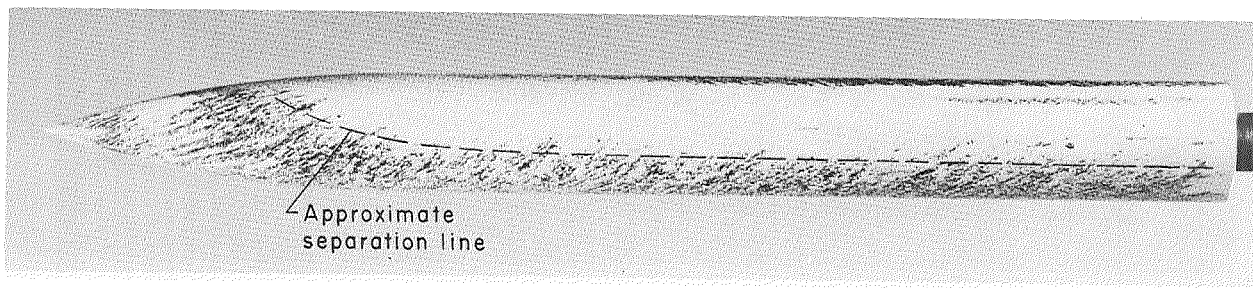


Figure 18.- Flow patterns resulting from sublimation tests of bodies at $\alpha = 0^\circ$; $M_\infty = 1.98$, $R = 6.7 \times 10^6$.

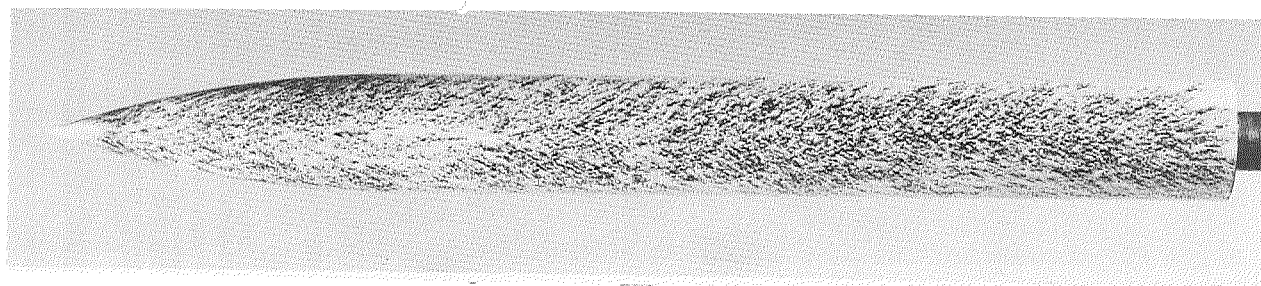
Top



Side



Bottom



B₁ ○

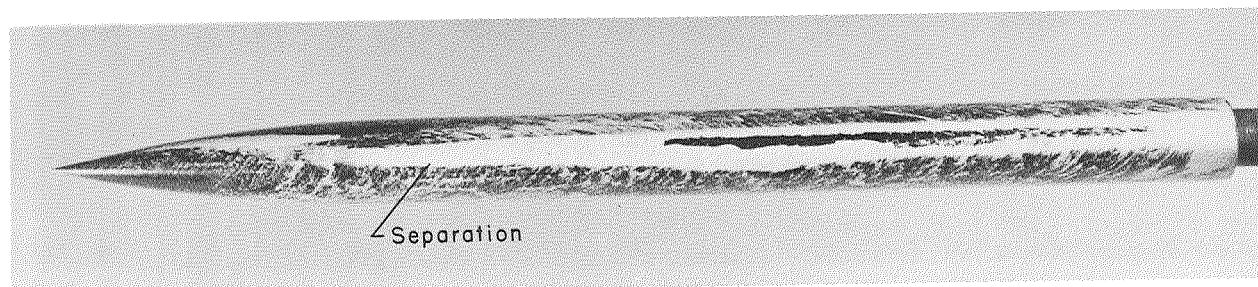
(a)

Figure 19.- Flow patterns resulting from white-lead tests of bodies at $\alpha = 10^\circ$; $M_\infty = 1.98$,
 $R = 6.7 \times 10^6$.

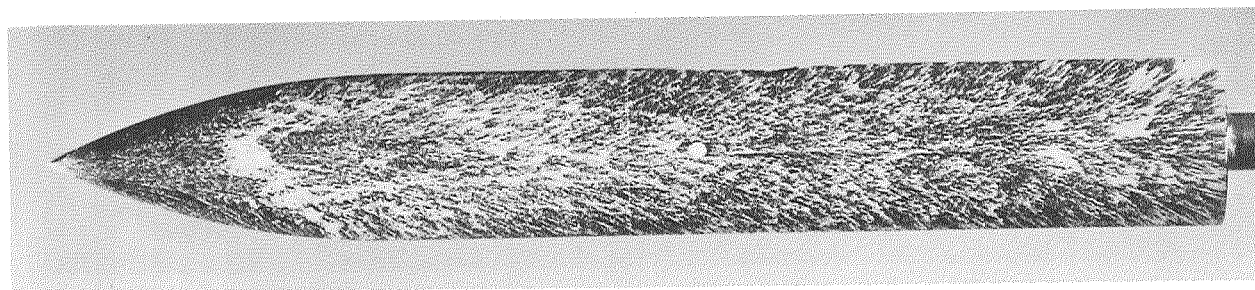
Top



Side



Bottom

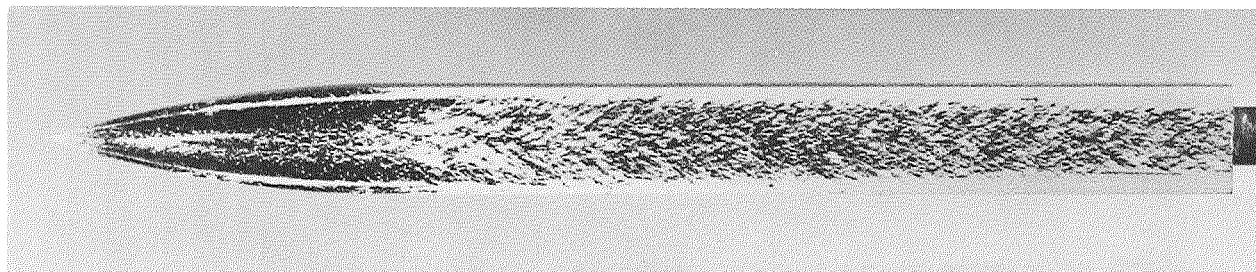


$$B_3, \frac{a}{b}=2 \quad \bigcirc$$

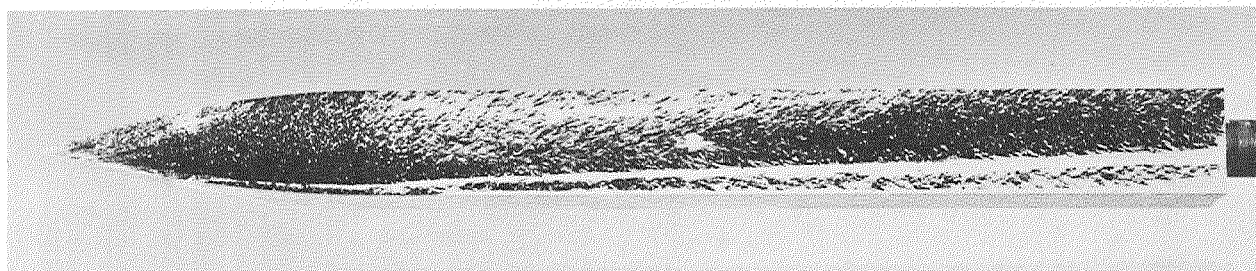
(b)

Figure 19.- Continued.

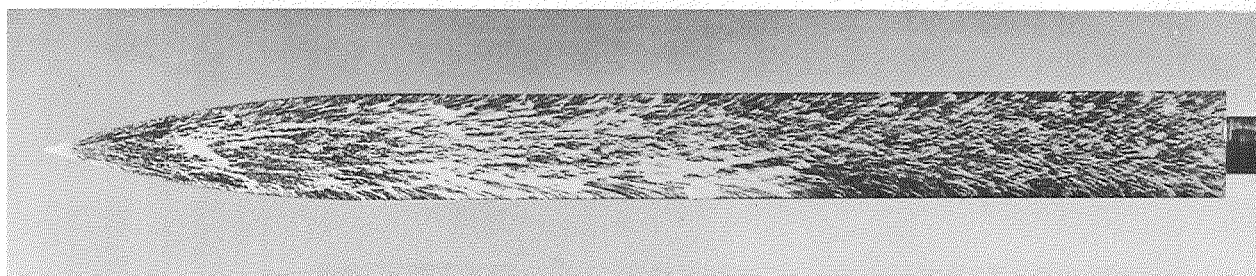
Top



Side



Bottom

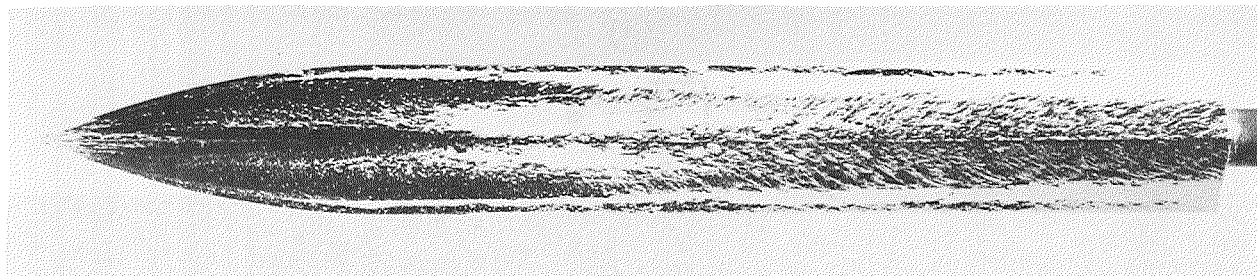


B₄ 

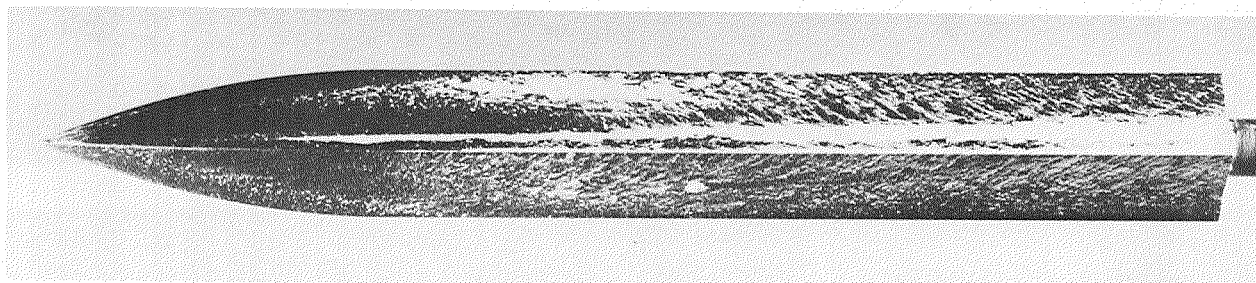
(c)

Figure 19.- Continued.

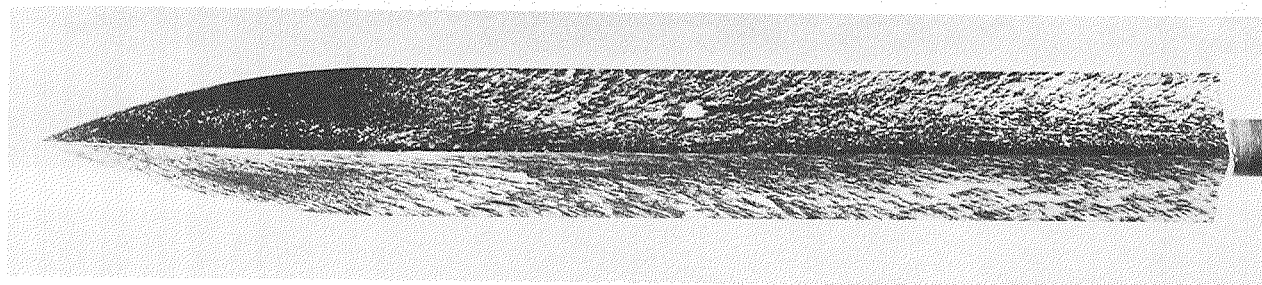
Top



Side



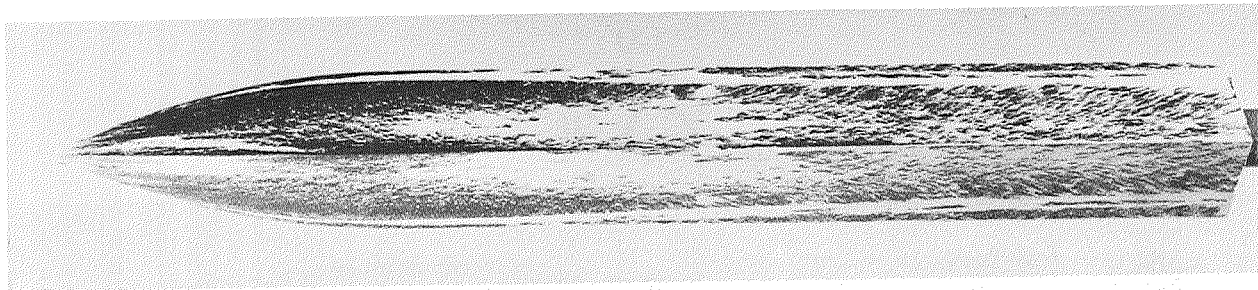
Bottom

B₄ 

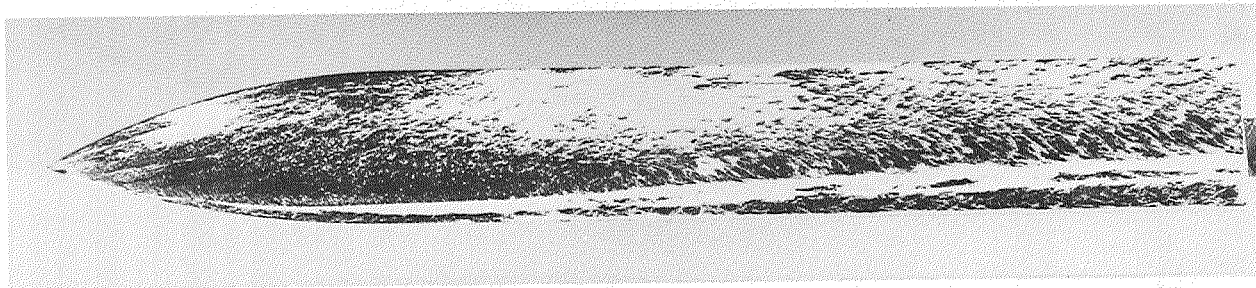
(d)

Figure 19.- Continued.

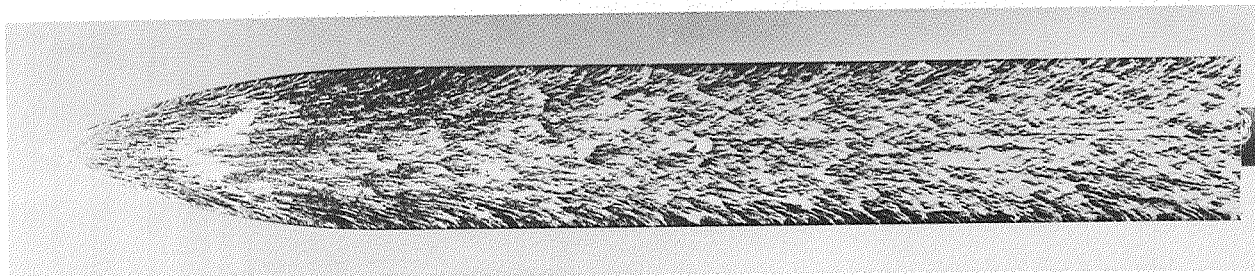
Top



Side



Bottom




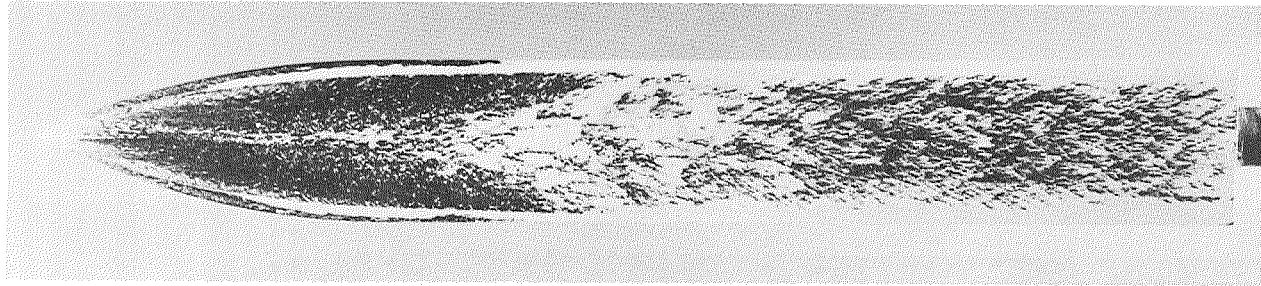
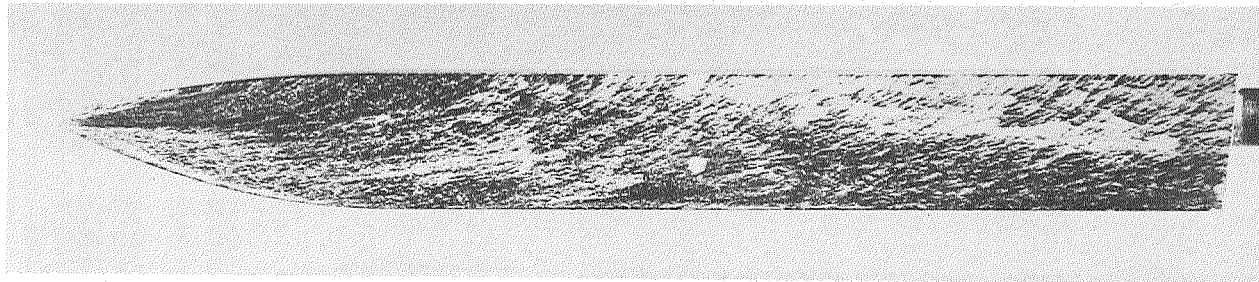
B₅ 
(e)

Figure 19.- Continued.

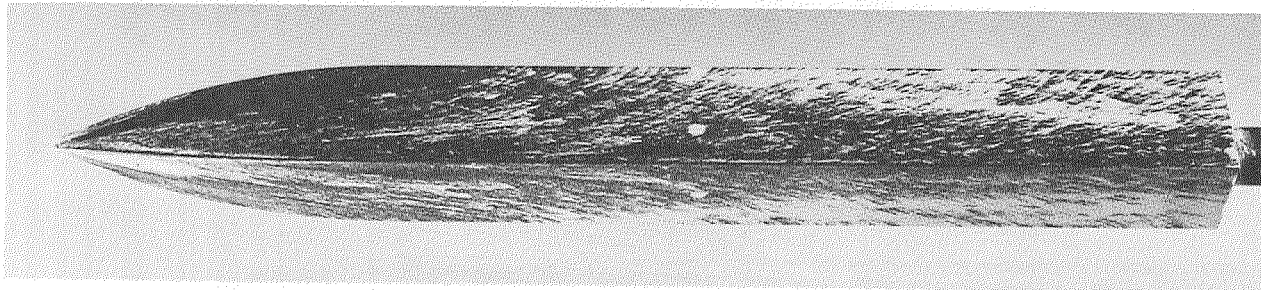
Top



Side



Bottom




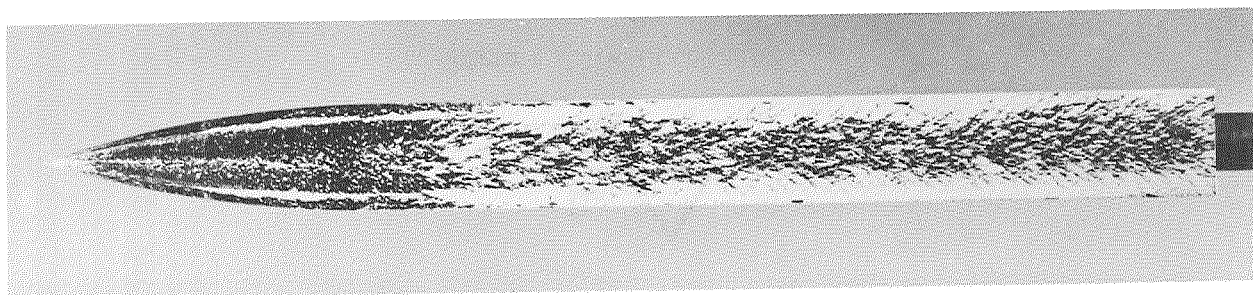
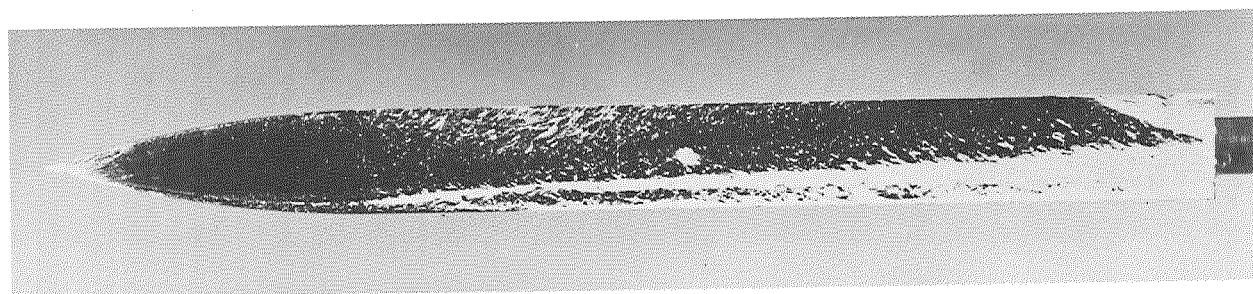
B₅ 
(f)

Figure 19.- Concluded.

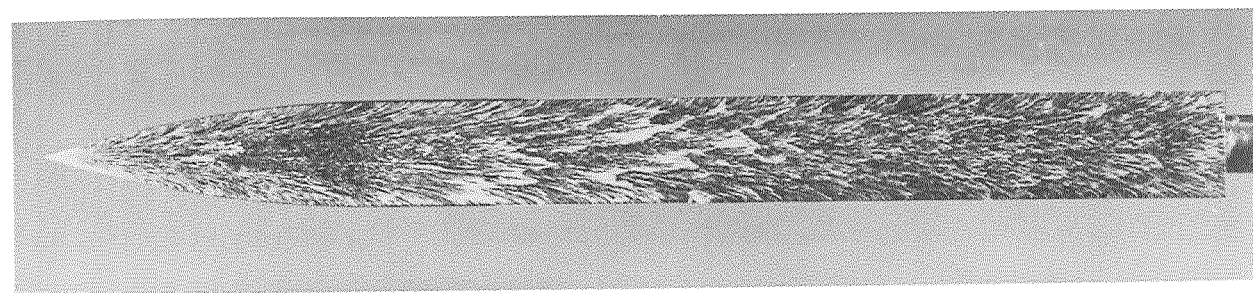
Top



Side



Bottom

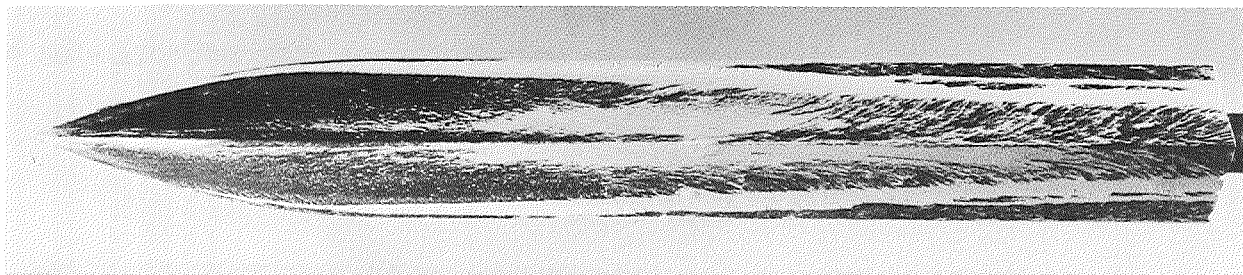


B₄ 

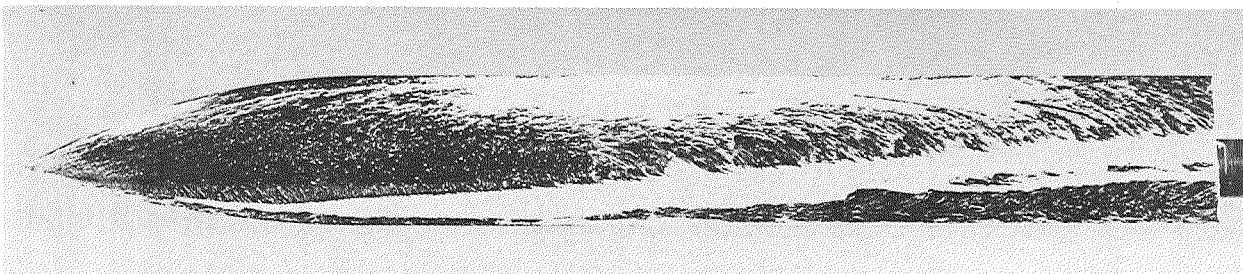
(a)

Figure 20.- Flow patterns resulting from white-lead tests of bodies at $\alpha = 14^{\circ}$; $M_{\infty} = 1.98$,
 $R = 6.7 \times 10^6$.

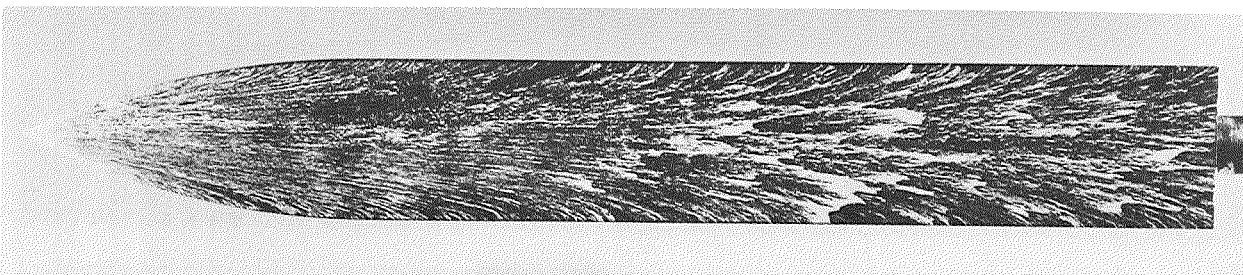
Top



Side

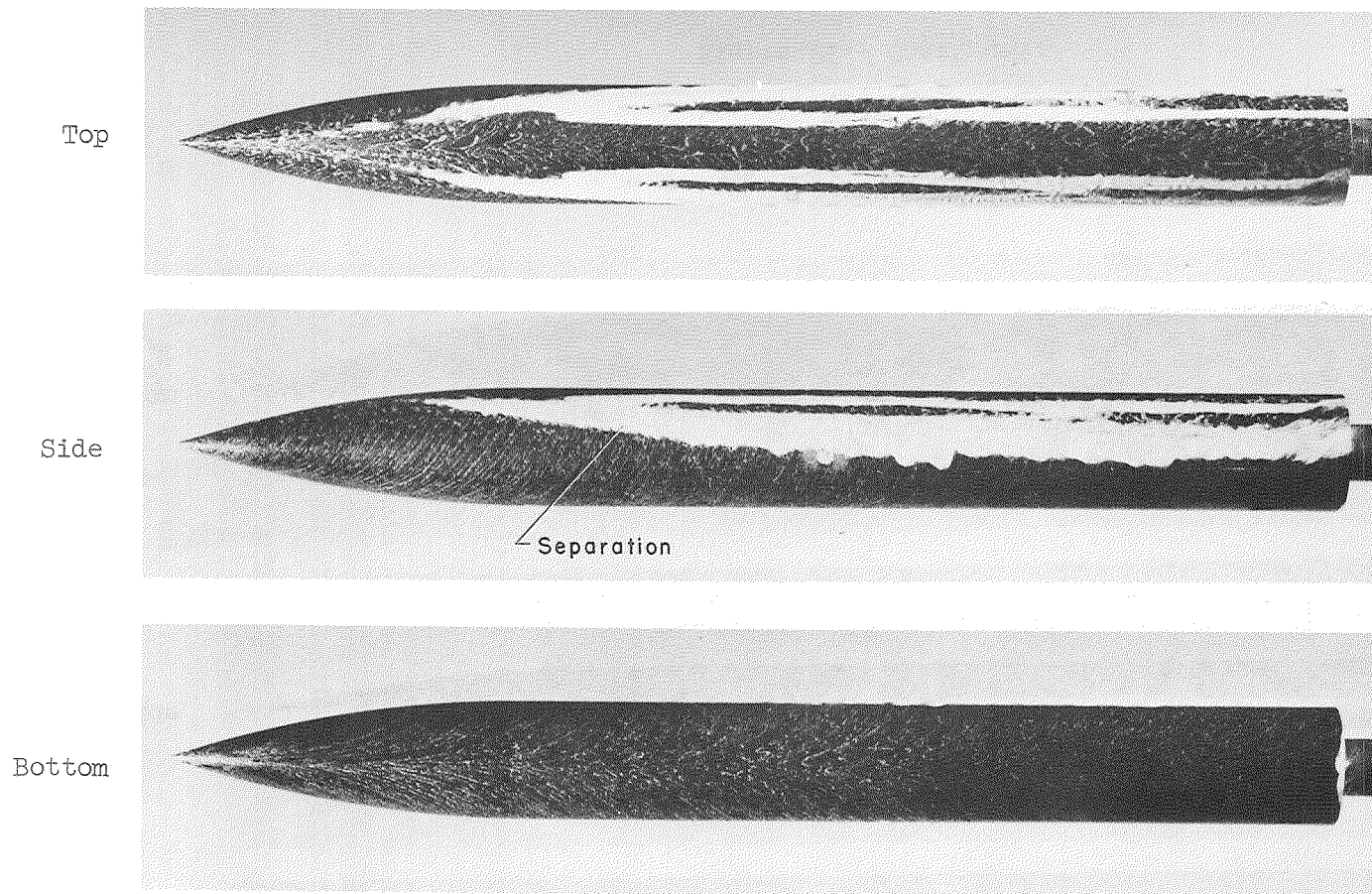


Bottom

 B_5 

(b)

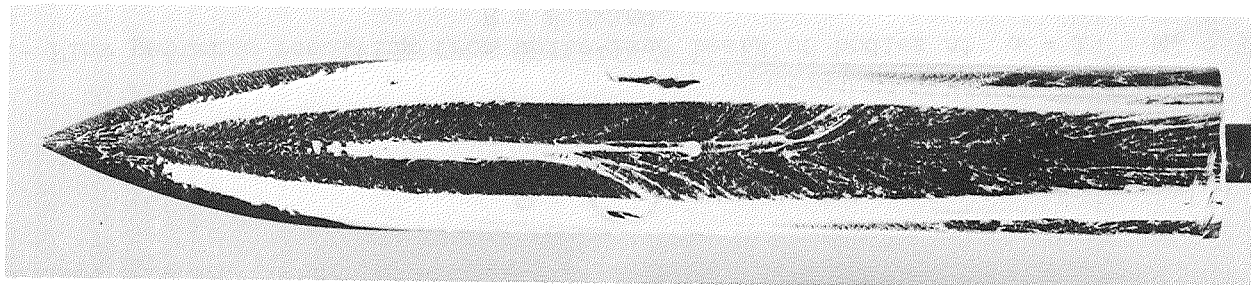
Figure 20.- Concluded.



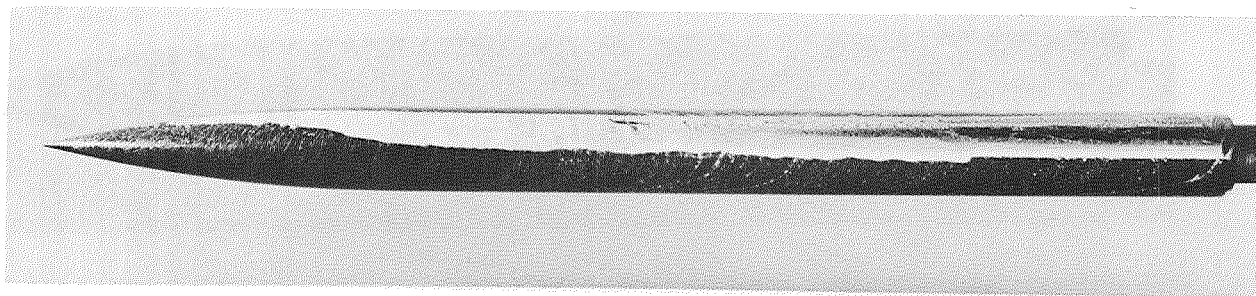
B_1 ○
(a)

Figure 21.- Flow patterns resulting from white-lead tests of bodies at $\alpha = 14^\circ$; $M_\infty = 3.88$,
 $R = 6.7 \times 10^6$.

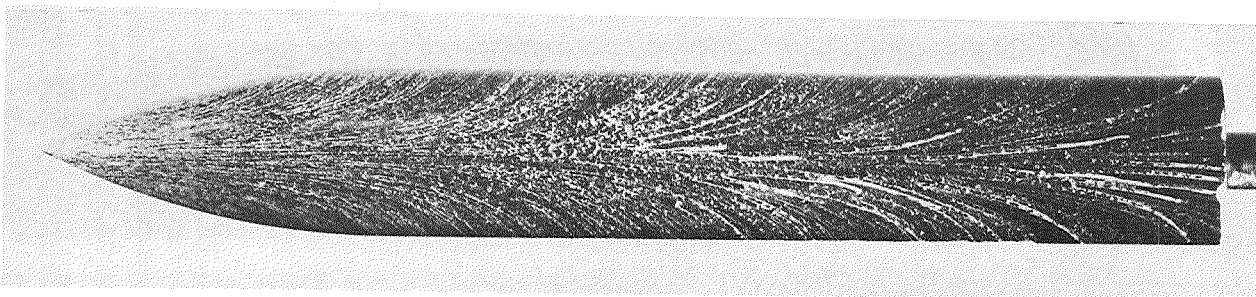
Top



Side



Bottom

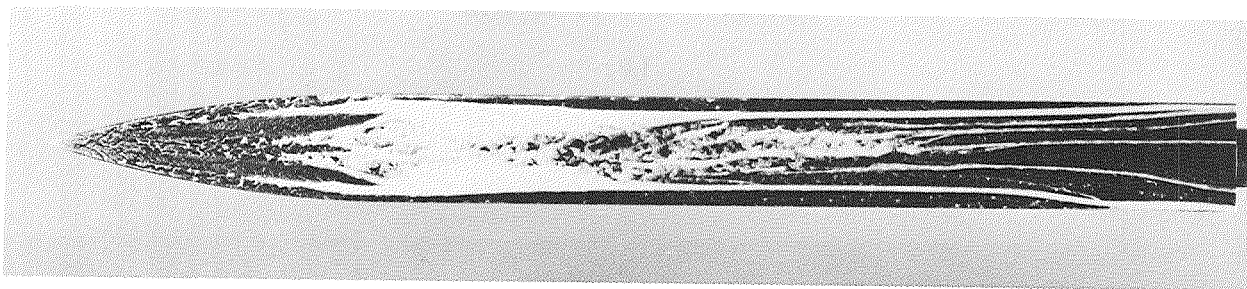


$$B_3, \frac{a}{b} = 2 \quad \bigcirc$$

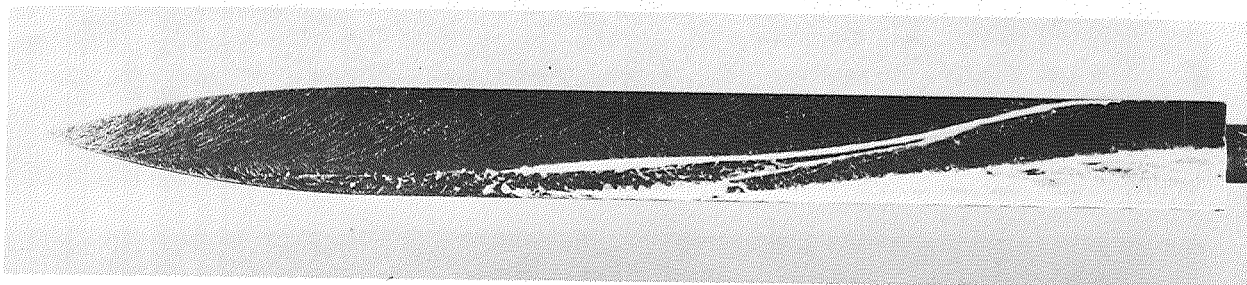
(b)

Figure 21.- Continued.

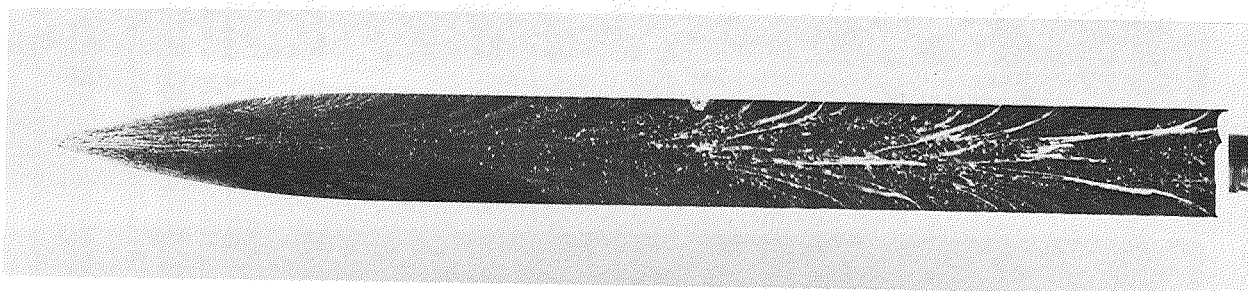
Top



Side



Bottom



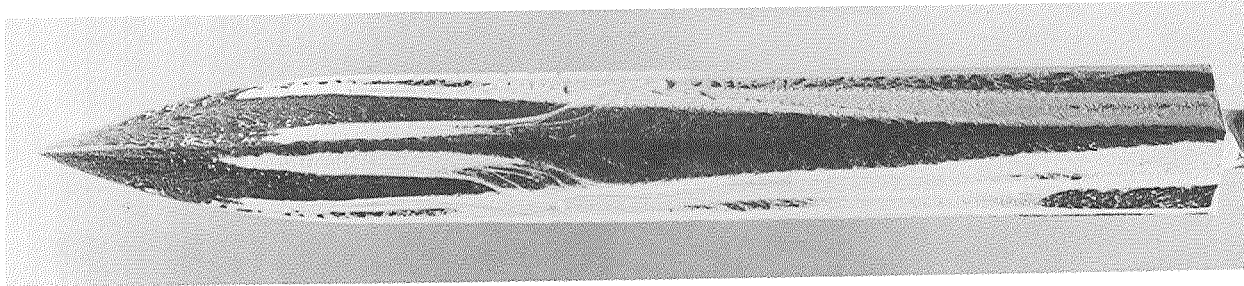
B₄



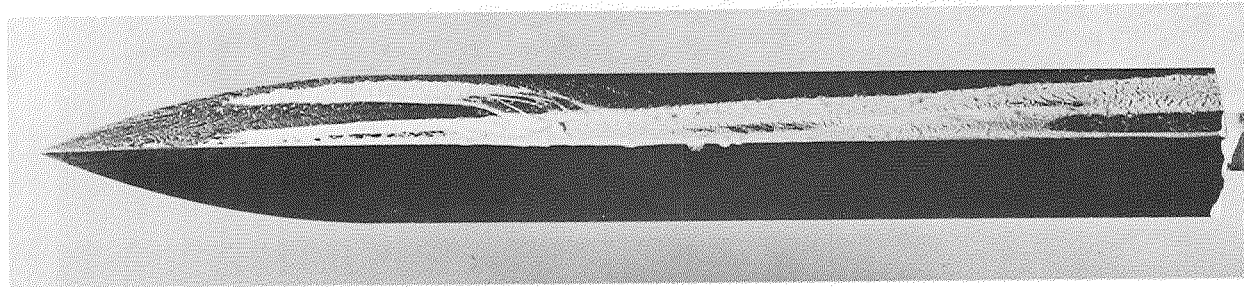
(c)

Figure 21.- Continued.

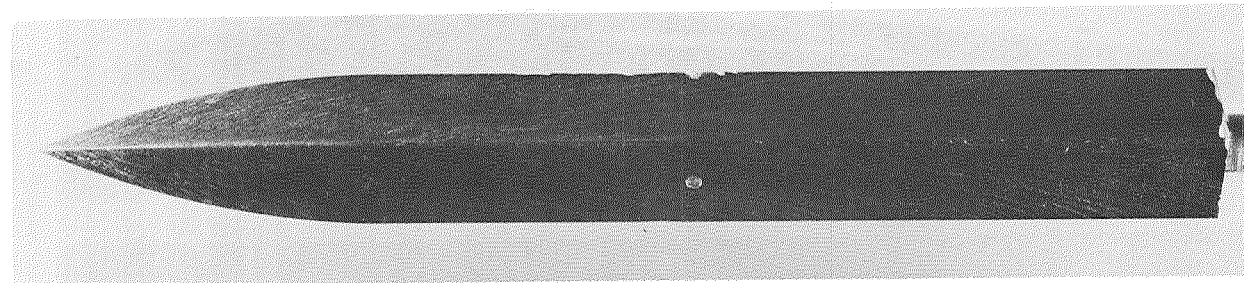
Top



Side



Bottom




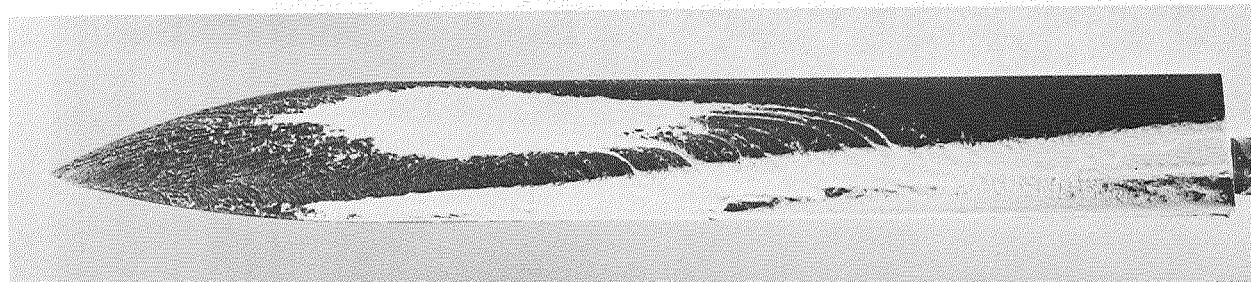
B₄ 
(d)

Figure 21.- Continued.

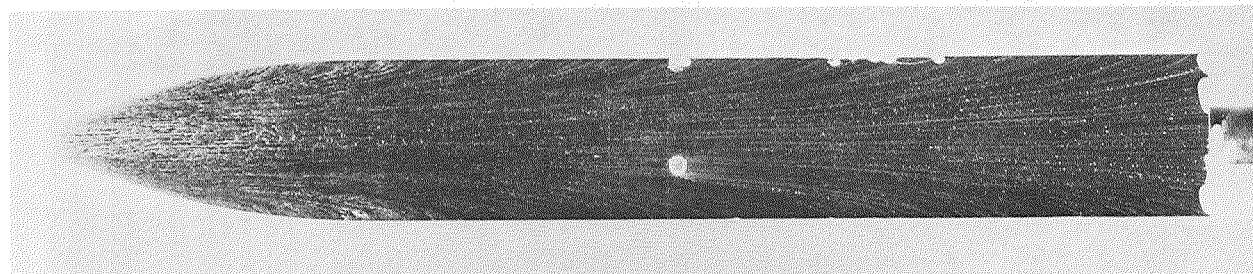
Top




Side



Bottom

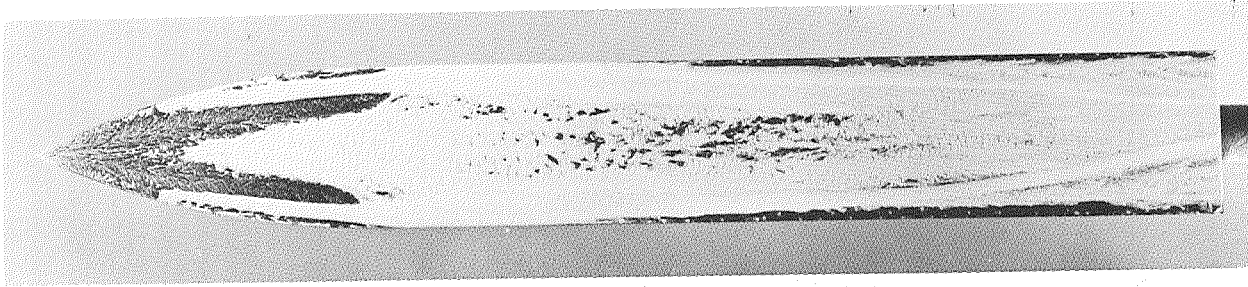


B₅ 

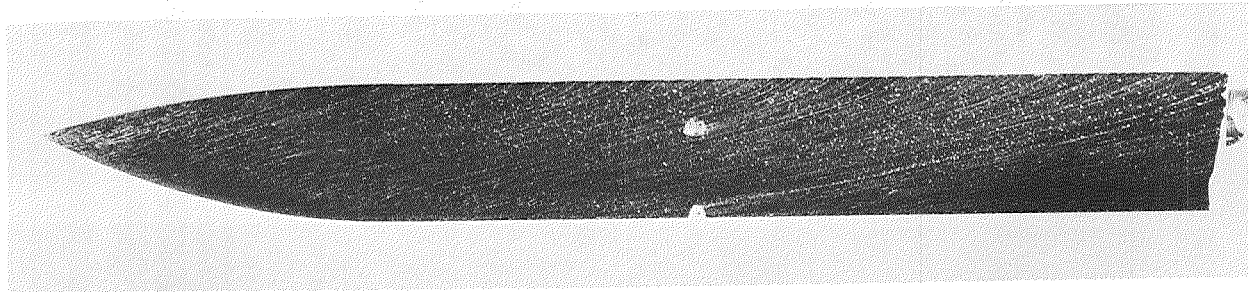
(e)

Figure 21 - Continued.

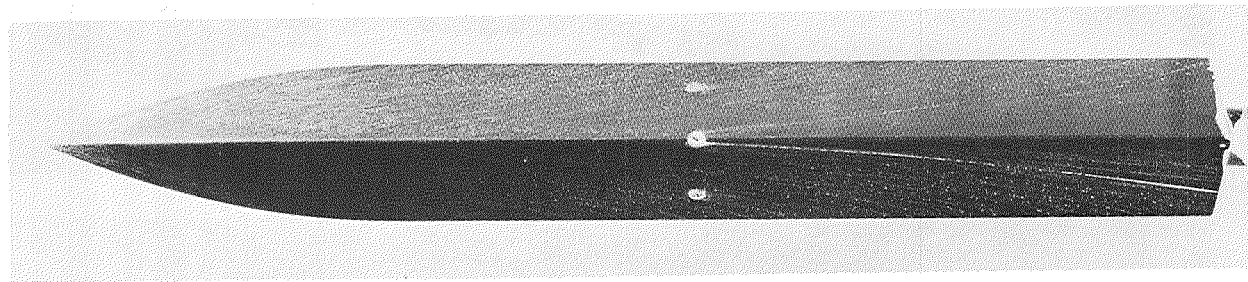
Top




Side



Bottom



B₅ 

(f)

Figure 21.- Concluded.